

# Microrobotic Swarms for Intracellular Measurement with Enhanced Signal-to-Noise Ratio

Xian Wang,<sup>#</sup> Tiancong Wang,<sup>#</sup> Xin Chen, Junhui Law, Guanqiao Shan, Wentian Tang, Zheyuan Gong, Peng Pan, Xinyu Liu, Jiangfan Yu, Changhai Ru,<sup>\*</sup> Xi Huang,<sup>\*</sup> and Yu Sun<sup>\*</sup>



Cite This: <https://doi.org/10.1021/acsnano.2c02938>



Read Online

ACCESS |



Metrics & More



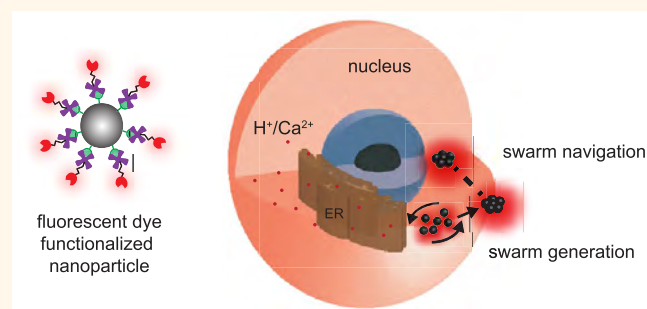
Article Recommendations



Supporting Information

**ABSTRACT:** In cell biology, fluorescent dyes are routinely used for biochemical measurements. The traditional global dye treatment method suffers from low signal-to-noise ratios (SNR), especially when used for detecting a low concentration of ions, and increasing the concentration of fluorescent dyes causes more severe cytotoxicity. Here, we report a robotic technique that controls how a low amount of fluorescent-dye-coated magnetic nanoparticles accurately forms a swarm and increases the fluorescent dye concentration in a local region inside a cell for intracellular measurement. Different from existing magnetic micromanipulation systems that generate large swarms (several microns and above) or that cannot move the generated swarm to an arbitrary position, our system is capable of generating a small swarm (e.g., 1  $\mu\text{m}$ ) and accurately positioning the swarm inside a single cell (position control accuracy: 0.76  $\mu\text{m}$ ). In experiments, the generated swarm inside the cell showed an SNR 10 times higher than the traditional global dye treatment method. The high-SNR robotic swarm enabled intracellular measurements that had not been possible to achieve with traditional global dye treatment. The robotic swarm technique revealed an apparent pH gradient in a migrating cell and was used to measure the intracellular apparent pH in a single oocyte of living *C. elegans*. With the position control capability, the swarm was also applied to measure calcium changes at the perinuclear region of a cell before and after mechanical stimulation. The results showed a significant calcium increase after mechanical stimulation, and the calcium increase was regulated by the mechanically sensitive ion channel, PIEZO1.

**KEYWORDS:** Micro/Nano Robotics, Micromanipulation, Swarm, Fluorescent Imaging, Signal-to-Noise Ratio



Fluorescent dyes are routinely introduced into cells in cell biology for measuring pH, ion concentrations, temperature, etc. of the intracellular environment.<sup>1–3</sup> In fact, the majority of measurements in cell biology rely on fluorescent intensity readout.<sup>4–8</sup> However, many fluorescent dyes, especially when used for detecting a low concentration of ions, suffer from low signal-to-noise ratios (SNR), and increasing the imaging laser's intensity for stronger fluorescent signals causes photobleaching and sample damage.<sup>9,10</sup> Furthermore, many biochemical constructs of fluorescent dyes are toxic to cells, especially when used in a high dose for increasing the SNR.<sup>11–13</sup> When a fluorescent dye is not cell membrane permeable, micelles and liposomes can be used to transport fluorescent dyes to a target cellular structure,<sup>14,15</sup> although the SNR can be increased locally, the issue of increased cytotoxicity persists. Thus, it is desired to introduce a low amount of fluorescent dyes into a cell for lower toxicity

and on-demand concentrate the fluorescent dyes in the region of interest in a cell for locally increasing the SNR.

Magnetic nanoparticles can be coated with various types of fluorescent dyes for measurement, with the advantage of high surface-area-to-volume ratio and the convenience of magnetic separation.<sup>16,17</sup> Recent works also employed genetic approaches to synthesize ferritin, a natural protein cage, as an intracellular magnetite for fluorescent localization and manipulation.<sup>18</sup> Different from global dye treatment to the cell with a high dose of fluorescent dyes as presently practiced

**Received:** March 24, 2022

**Accepted:** June 28, 2022

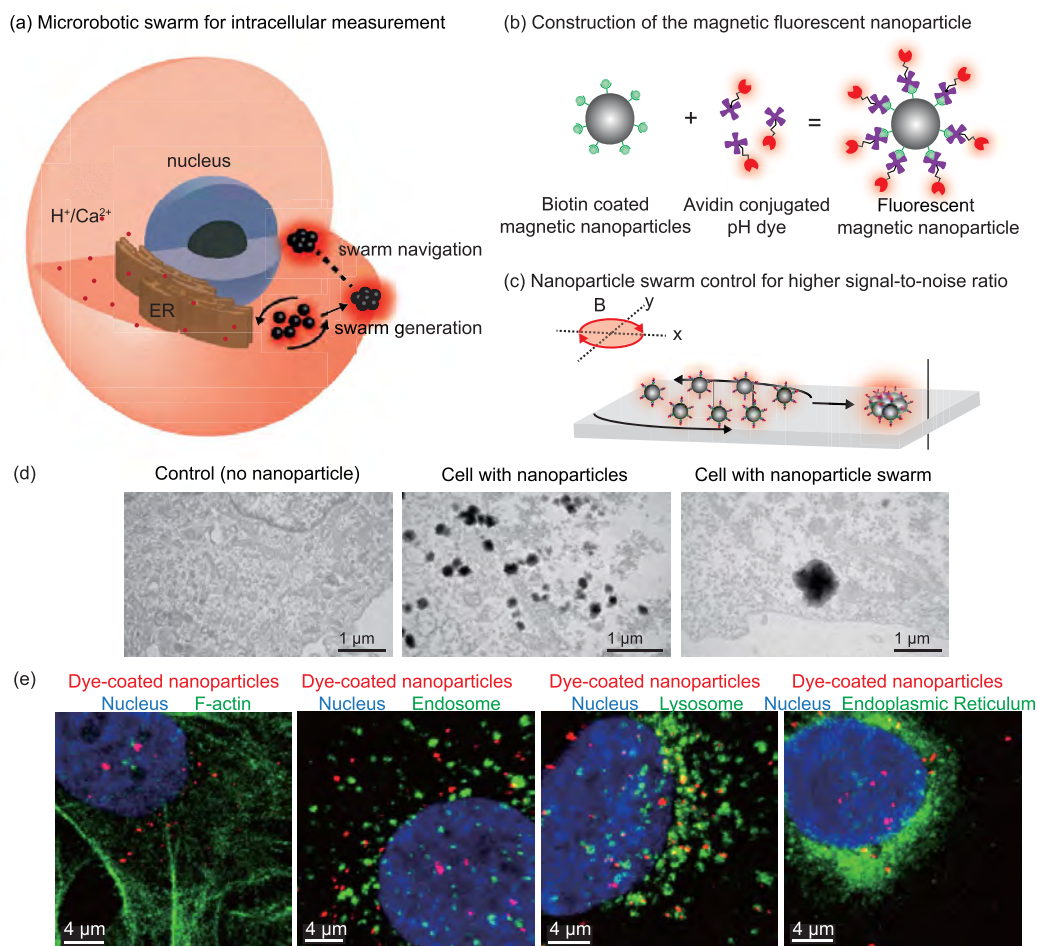


**Figure 1.** (a) Schematic of intracellular measurement using a microrobotic swarm. A swarm composed of magnetic nanoparticles is formed and controlled to navigate to different locations inside a cell. (b) Construction of the magnetic fluorescent nanoparticle. Magnetic nanoparticles were coated with biotin and then with avidin pHrodo red dyes through avidin–biotin binding. (c) Swarm of fluorescent nanoparticles increasing the local signal-to-noise ratio. (d) Transmission electron microscope images of the intracellular nanoparticles and an intracellular swarm. (e) Co-staining of intracellular organelles and nanoparticles (red color) after endocytosis. The results showed that the nanoparticles were not trapped in the cytoskeletal network or internalized into the intracellular membrane-bounded organelles (endosome, lysosome, endoplasmic reticulum, Golgi apparatus, and mitochondria).

in cell biology measurements, our approach involves the manipulation of fluorescent-dye-coated magnetic nanoparticles to form a swarm/aggregate of a controllable size and locally enrich the concentration of fluorescent dyes for a higher SNR [Figure 1a–c, Supplementary Video S1]. In addition to the increased SNR, only a small amount of dye needs to be introduced into a cell, resulting in reduced toxicity to the cell. Through magnetic field control of the size and position of the swarm, the swarm of fluorescent-dye-coated magnetic particles can be moved to different locations inside the cell to perform measurements [Figure 1a].

Magnetic micromanipulation has been applied to intracellular studies. For example, a single submicron magnetic particle was controlled to navigate inside a cell and perform mechanical measurement on the cell nucleus in situ,<sup>19</sup> magnetic nanoparticles were mobilized in the cytosol for quantifying intracellular viscosity,<sup>20</sup> magnetic nanoparticles were attached onto the cell surface to generate mechanical stimulation through force and clustering,<sup>21</sup> and fluorescently labeled magnetic nanoparticles were used for intracellular localization and imaging.<sup>22</sup> Although intracellular motors, helical swimmers, nanowires, and functionalized single

magnetic beads have been proven to be effective for intracellular delivery, navigation and fluorescent detection, swarm generation and position control of these intracellular magnetites (motors, nanoparticles, nanowires, helical swimmers) have yet to be explored.

To perform intracellular measurement using a magnetic swarm, the swarm must be small in size (e.g., 1  $\mu\text{m}$ ) considering the size of a cultured cell ( $\sim 10 \mu\text{m}$ ); additionally, the position of the swarm needs to be controlled to perform measurement in different target locations inside the cell. Existing magnetic swarm control techniques include gradient-based and field strength-based methods. The gradient-based swarm control technique utilizes the attractive force generated by magnetic coils and poles acting on magnetic particles.<sup>23–25</sup> Multiple poles have been used to control the position of a single magnetic microparticle.<sup>26–28</sup> However, for swarm formation, magnetic particles are aggregated near the coil (or pole tips), and the swarm cannot be moved to an arbitrary location in the workspace or inside a cell. Thus, the gradient-based method is not suitable for controlling a swarm to perform intracellular measurement.

The field strength-based technique controls magnetic particles to form chains; then the chains rotate to form a disk-shaped swarm by fluidic vortices generated by neighboring chains. The formed swarm can be navigated to a target position through tumbling or rolling along the substrate's surface.<sup>29</sup> Existing systems focused on position control of a swarm for transportation applications. A rotating magnetic field was generated in a workspace of several millimeters, and swarms ranging from tens of micrometers<sup>30,31</sup> to several hundreds of micrometers<sup>32,33</sup> were formed. In these systems, small swarms were generated and then merged to form larger swarms through the interactions with fluidic vortices. Such large-sized swarms are not suitable for performing intracellular measurements.

Multipole magnetic tweezers generate a focused magnetic field near the sharp tips. Recent studies used multipole magnetic tweezers to control the position of a single magnetic particle at the micro and submicron scale in the fluidic environment,<sup>27</sup> inside a mouse embryo,<sup>34</sup> and inside a single cell for mechanical measurement.<sup>26</sup> However, each of the poles was stationary. Thus, the magnetic particle can only move toward the dominating pole, and no local maximum field strength can be generated in between the poles to form a swarm of nanoparticles. Including an additional movable pole would enable the generation of local maximum field strength within the 2D plane through controlling the magnetic field in 3D, which would further enable the formation of a micrometer-sized swarm of nanoparticles in an arbitrary location in the workspace.

This paper presents a field strength-based system and technique capable of both position and size control of a magnetic swarm for intracellular measurement. We designed a five-pole magnetic device, consisting of four stationary coils and one movable coil, which generates a highly focused rotating magnetic field in the workspace ( $400\ \mu\text{m} \times 400\ \mu\text{m}$ ) where cells are seeded. Our developed magnetic field model and particle dynamics model relate the position of the movable coil to the position of the formed swarm, and electric current is applied to the coils to the size of the swarm. The system was able to generate a magnetic swarm from  $0.52$  to  $52.7\ \mu\text{m}$  with an error  $<7.5\%$  and position the swarm with an accuracy of  $0.76\ \mu\text{m}$ . The robotic controlled magnetic swarm performed intracellular pH measurement along a trajectory from the leading edge to the trailing edge (spatial) inside a migrating cell, and performed intracellular calcium measurement at the perinuclear region before and after mechanical stimulation (temporal). It significantly increased the local SNR inside a cell compared with results for the traditional global dye treatment method. The intracellular measurement results quantitatively revealed the existence of apparent pH gradient in live migrating cells; and  $\text{Ca}^{2+}$  distributions at the perinuclear region in response to mechanical stimulation. The technique was also applied to measuring the intracellular apparent pH value within the oocytes of living *C. elegans*, demonstrating its capability for intracellular measurement in vivo.

## RESULTS AND DISCUSSION

**Fluorescent Magnetic Nanoparticles and Intracellular Distribution.** When the size of magnetic particles increases, their surface-area-to-volume ratio decreases, limiting the surface coating efficiency for the same amount/weight of magnetic particles.<sup>35,36</sup> Larger particles can reduce cell viability.<sup>26,37,38</sup> For smaller magnetic particles, magnetic

gradient force decreases with size by the power of four, limiting their aggregation and separation capabilities.<sup>26</sup> Taking into account the trade-off between magnetic force scaling, surface coating efficiency, and cell viability after microinjection of particles, we chose magnetic particles with a diameter of  $130\ \text{nm}$  ( $124 \pm 5\ \text{nm}$ ; permeability,  $1.615 \times 10^{-6}\ \text{H/m}$ ; nanomag-D, Micromod, Germany). The particles were first coated with adhesion molecule biotin and then paired with the adhesion molecule avidin [Figure 1b,c]. Used as examples, three types of dyes, avidin-Alexa 555 for intracellular localization, pHrodo red for measuring intracellular pH (proton concentration), and Cal-520 biotin for measuring intracellular calcium were used for coating. After the nanoparticle surface was functionalized with fluorescent sensors, the coated magnetic nanoparticles were examined by microscopy, and no observable aggregate larger than  $500\ \text{nm}$  was found. With no magnetic field applied, the SNR of the solution of dye-coated magnetic particles and that of the pH-sensitive dye solution were not significantly different ( $3.21 \pm 0.41$  vs  $3.01 \pm 0.40$ ,  $P = 0.48$ ,  $n = 5$  independent measurements). A similar functionalization was performed by using Cal-520 biotin conjugate to measure intracellular calcium, as shown in Figure S1.

The delivery of the nanoparticles can be through either endocytosis or microinjection. The endocytosis process is cell-type and material dependent. For example, fast-proliferating cells are more inclined to internalize particles whereas differentiated cells have poorer endocytosis capability.<sup>39–41</sup> Furthermore, the nanoparticles endocytosed into the cell can be captured within membrane-bound organelles such as endosome and lysosome, and membrane lysis of these organelles for the nanoparticles to enter the cell's cytoplasmic environment can impact cell metabolism.<sup>42</sup> Thus, in this work, we chose to use microinjection to deliver a controlled amount of nanoparticles into the cytoplasm.

Microinjection was performed at the center of the cell with an injection depth of  $0.5\ \mu\text{m}$  to deliver the nanoparticles into cytoplasm. Before the swarm was used for intracellular measurement, the localization of nanoparticles inside cells was investigated. Figure 1d shows transmission electron microscopy (TEM) images of magnetic nanoparticle distribution (without applying magnetic field) and a swarm (after applying magnetic field) inside a cell. To further investigate where the nanoparticles locate within the cell after microinjection, intracellular organelles were costained. From confocal microscopy imaging, as shown in Figure 1e, it was observed that the nanoparticles spread within the cytoplasmic environment after microinjection. 3D image data showed that the nanoparticles were outside the nucleus. The 3D confocal images also revealed that the nanoparticles were not trapped by the cytoskeletal network, and there were no nanoparticles found within the endosome, lysosome, and endoplasmic reticulum. Because of van der Waals interactions, there were small clusters of nanoparticles within the cytoplasm formed by nonspecific aggregation. Overall, the results showed that the nanoparticles mostly localized in the cytoplasm, enabling their free motion in the cell.

**Micro-Swarm Robotic System.** To generate an aggregate/swarm of magnetic particles and control its position, we built a magnetic device with four stationary coils and one movable coil [Figure S2a], placed on an inverted microscope. Electron discharge machining (EDM) of a high-permeability foil sheet (MuShield, USA) was used to produce the four stationary poles with sharp tips (diameter,  $2.88\ \mu\text{m}$ ; thickness,

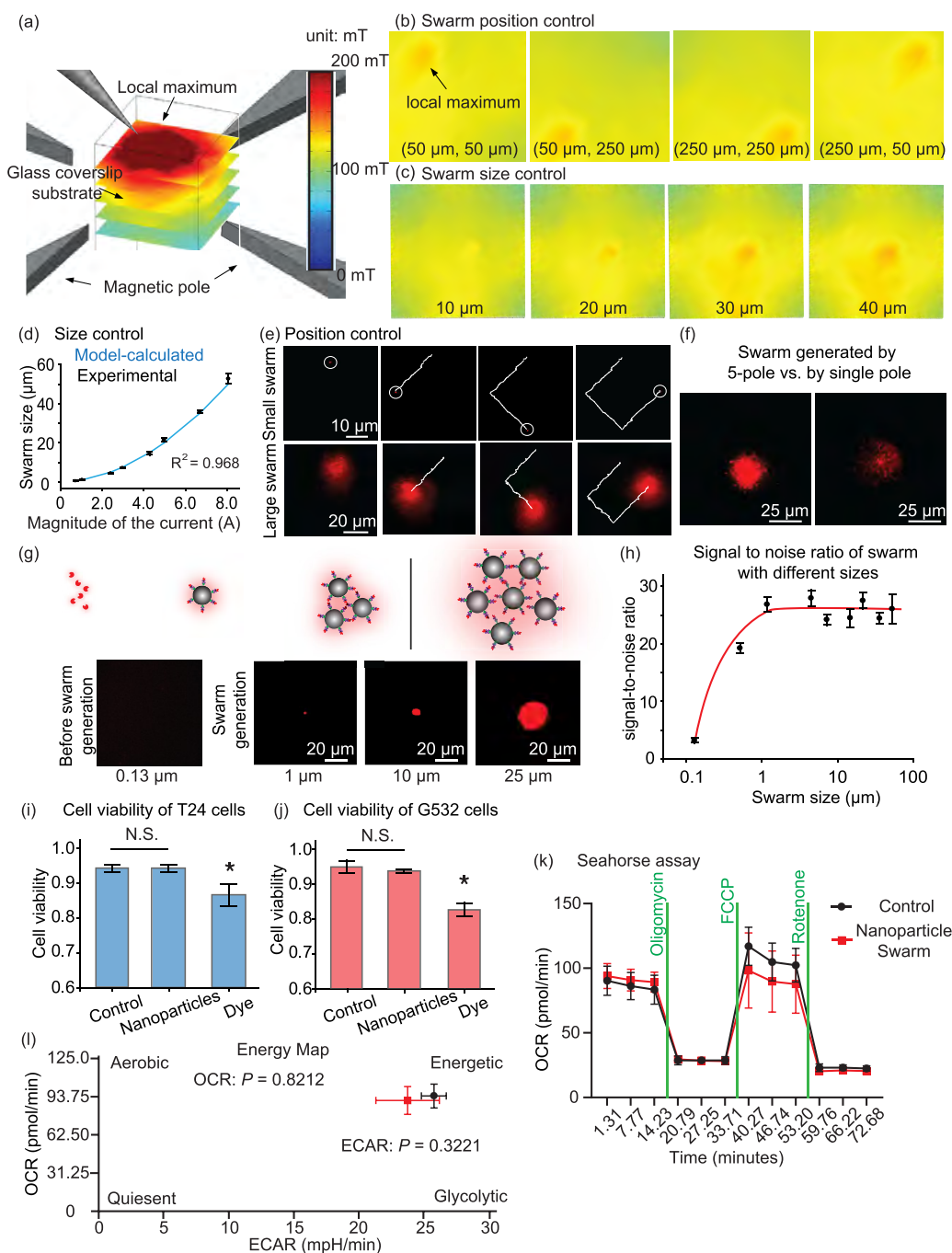


**Figure 2.** (a) Magnetic field simulation of the five-pole magnetic system. Five magnetic poles generate a 3D magnetic field, and a local maximum field strength appears in multiple 2D planes. (b) Position control of the region with a magnetic field strength larger than 130 mT, where magnetic fluorescent nanoparticles form a swarm on the basis of eq 9. (c) Swarm size control through controlling the size of the region with a magnetic field strength larger than 130 mT. The finite element simulation model was built in COMSOL using the same device geometries, with a supplied current of 2 A for each of the stationary coils and  $-2$  A for the mobile coil. The Z position of the planes shown in (b) and (c) is the plane of the coverslip's top surface, i.e., where cells are seeded, as indicated in (a). (d) Swarm size control through controlling the current in each of the coils, based on the model in eq 4 and eq 10. (e) Position control of a small swarm (1  $\mu\text{m}$ ) and a large swarm (25  $\mu\text{m}$ ). (f) Comparison of a 25  $\mu\text{m}$  swarm generated by our five-pole magnetic tweezers (left) and by single-pole magnetic tweezers (right). (g) Swarms formed by magnetic fluorescent nanoparticles. (h) Local signal-to-noise ratio increase with the increase of the swarm size. (i), (j) Cell viability test.  $n = 3$  independent cell counting experiments. Error bar: standard deviation. Fluorescent magnetic nanoparticles delivered by microinjection exhibited no significant toxicity to the cells whereas the dye generating the same signal-to-noise ratio showed more significant toxicity compared to results for the control group. (k), (l) Cell metabolism tests performed to compare the cell metabolism activities before and after magnetic micromanipulation. The results showed no significant change of the cell metabolism state before and after the magnetic nanoparticle swarm measurement (quantified by using oxygen consumption rate (OCR),  $P = 0.8212$ , extracellular acidification rate (ECAR),  $P = 0.3221$ , and  $n = 4$  independently repeated experiments).

150  $\mu\text{m}$ ). The four coils were wired onto a magnetic yoke to synchronize the four stationary coils to generate a rotating magnetic field. The four coils were placed 400  $\mu\text{m}$  between each pair to leave a sufficient workspace for cell imaging. The movable pole was made from an iron rod and fabricated by lathing; it was then further machined by EDM to produce a cylindrical tip (diameter: 21.23  $\mu\text{m}$ ). Magnetic wire (Magnetic Wire, Gauge 14, Digikay) was wired onto the movable pole. The movable pole was mounted on a robotic micro-manipulator with a positioning accuracy of 0.2  $\mu\text{m}$  along the XYZ axes. For experimental comparison of the multipole magnetic tweezers and single-pole magnetic tweezers, only the movable pole was used in the single-pole tweezers case. The five-pole magnetic device was controlled by a host computer through DAQ (NI-USB6211) and custom-made current amplifiers [Figure S2b]. For swarm position control in a cell, a target position (e.g., leading edge inside the cell) was user specified in the control software interface. The magnetic models described in the next section were used to control the current supplied to each coil, and the robotic micro-manipulator was controlled with real-time visual feedback from microscopy imaging [Figure S2c] to position the movable pole tip. The magnetic pole and yoke were designed to be far from the workspace to minimize the potential effect from the heat generated in the coils. Temperature simulation using COMSOL showed that the workspace temperature increased by 1.08  $^{\circ}\text{C}$  from the room temperature 22  $^{\circ}\text{C}$  after 5 min of continuous magnetic actuation. As shown in Figure S2d, the workspace of 400  $\mu\text{m} \times 400 \mu\text{m}$  has a uniform temperature, ranging from 23.08  $^{\circ}\text{C}$  to 23.09  $^{\circ}\text{C}$ .

Traditional single-pole magnetic tweezers are only able to provide one-directional attractive force, resulting in poor control of the shape and size of a swarm, as shown quantitatively in the next section. In existing multipole magnetic tweezers such as four-pole magnetic tweezers,<sup>43–45</sup> the maximum field strength is located near the tips of the poles, unsuitable for positioning a magnetic swarm to an arbitrary location inside a cell.<sup>46</sup> In contrast, our five-pole device, by placing a movable pole tip in a different plane (250  $\mu\text{m}$ ) above the four stationary poles, permits highly accurate control of the position and size of a magnetic swarm. When sinusoidal currents are supplied to the four stationary coils and the same sinusoidal current but with a phase difference of  $\pi$  is supplied to the movable coil, the maximum field strength is formed in a plane between the movable tip and the four stationary tips [Figure 2a, Figure S3]. When the micro-manipulator moves the movable pole, the region with maximum field strength changes accordingly [Figure 2b]. By control of the magnitude of the sinusoidal current, the size of the local maximum B region is regulated, forming a swarm of different sizes. In Figure 2c, one can see that the shape of large swarms (e.g., >30  $\mu\text{m}$ ) deviates more significantly from a spherical shape. This is because the movable pole is at a 45 $^{\circ}$  tilting angle relative to the stationary poles for accommodating the microscopy's light path [Figure S2a]. In experiments, the coverslip where cells were seeded was directly placed on the top surface of the stationary poles (coverslip thickness: 150  $\mu\text{m}$ ), as illustrated in Figure S2a. The Z distance between the cells and the movable pole tip was 100  $\mu\text{m}$ . Because the cell thickness was 3–5  $\mu\text{m}$ , the magnetic field strength along the Z direction inside a cell was largely the same.

**Magnetic Swarm Position and Size Control.** Existing magnetic models describe the mechanism of swarm formation;

i.e., chains of magnetic particles through interactions with fluidic vortices form a 3D aggregate/swarm.<sup>31–33</sup> To change the position of the formed swarm, the swarm needs to tumble or roll on a surface. However, cytoskeletal filaments in the cytoplasm prevent effective interactions of magnetic nanoparticles dispersed in the cell with the substrate, making the existing models unsuitable for position control of a magnetic swarm inside a cell. In addition, existing models teach the generation of a uniform rotating magnetic field in the workspace but do not describe how to generate maximum magnetic field strength in a pinpointed location.

To control the size and position of a magnetic swarm, we first developed the magnetic field model for our five-pole magnetic device and then derived the relationship between magnetic field strength and swarm size. According to the Gauss law of magnetism, each magnetic pole with a sharp tip can be represented by a magnetic charge,  $q$ .<sup>34,43</sup> On the basis of superposition of five magnetic charges, the magnetic field strength generated by our five-pole magnetic device is

$$\mathbf{B} = \sum_{j=1}^6 \left( \frac{\mu_0 q_j}{4\pi r_j^2} \mathbf{u}_j \right) = \sum_{j=1}^5 \frac{k_m q_j}{r_j^2} \mathbf{u}_j \quad (1)$$

where  $k_m = \mu_0/4\pi$  and  $\mu_0$  is the permeability of vacuum,  $r_j$  and  $\mathbf{u}_j$  represent the distance from a position in the workspace to the magnet charges and the unit vector in that direction, respectively. The magnetic moment of magnetic nanoparticles magnetized by the field is

$$\mathbf{m}_b = \frac{3V}{\mu_0} \left( \frac{\mu - \mu_0}{\mu + 2\mu_0} \right) \mathbf{B} \quad (2)$$

where  $\mu$  is the permeability of the magnetic nanoparticles and  $V$  is the nanoparticle's volume.

According to magnetic circuit analysis,<sup>43</sup> the magnetic charge value depends on the current in the coil, i.e.,

$$[q_1, q_2, q_3, q_4, q_5]^T = \frac{\Phi}{\mu_0} = \frac{n}{\mu_0 R_{\text{mag}}} \mathbf{K}_I \quad (3)$$

where  $\Phi$  is the matrix of magnetic flux produced by each magnetic charge,  $n$  represents the number of turns in each coil, and  $R_{\text{mag}}$  is the magnetic reluctance, determined by the magnetic properties of the poles, yoke, and cell medium.  $\mathbf{K}_I$  is a five-by-five distribution matrix of the magnetic flux. Substituting eq 3 into eq 1 results in

$$\mathbf{B} = \frac{nk_m}{\mu_0 R_{\text{mag}}} \sum_{j=1}^5 \mathbf{u}_j \frac{1}{r_j^2} \mathbf{K}_I \quad (4)$$

In our experiments, the field strength generated at a given position is controlled by controlling the current on the basis of eq 4. A sinusoidal current with the same magnitude, frequency, and zero phase angle was input into the four stationary coils, and the same sinusoidal current but with a phase angle of  $\pi$  was input into the movable coil. Thus, a rotating magnetic field was generated, and the magnetic field strength  $\mathbf{B}$  for each position in the workspace is determined by eq 4.

When magnetized, magnetic particles form chains because their magnetic moment is aligned to the same direction.<sup>47</sup> When a rotating magnetic field is applied, the chains rotate with the magnetic field. Through fluid vortex interactions among the chains of magnetic particles, the chains develop into a swarm/aggregate.<sup>32,33</sup> To maintain the shape of the swarm,

magnetic torque  $T_{\text{mag}}$  and fluid torque  $T_{\text{drag}}$  must be balanced; otherwise, the shear at the boundary of the swarm disassembles the swarm.

For a chain of length  $L$  that consists of  $N$  particles ( $L = 2Na$ , and  $a$  is the radius of a particle), the induced magnetic torque of a rotating chain can be obtained as a sum of all torques exerted by neighboring particles, i.e.,

$$T_{\text{mag}} = \frac{3\mathbf{m}_b^2}{4\pi\mu_0} \frac{N^2}{16a^3} \sin(2\alpha) \quad (5)$$

where  $\alpha$  is the phase lag between the applied rotating magnetic field and the rotation of the magnetic particle chains. Substituting eq 2 and eq 4 into eq 5 results in

$$T_{\text{mag}} = \frac{9\pi a^3 N^2 (\mu - \mu_0)^2}{4\mu_0^3 (\mu + 2\mu_0)^2} \mathbf{B}^2 \sin(2\alpha) \quad (6)$$

The fluid torque balancing the rotation of a chain is

$$T_{\text{drag}} = \kappa V \eta \omega \quad (7)$$

where  $\kappa = 2N^2 / \ln(\frac{N}{2})$  is a shape factor,<sup>47</sup>  $V = \frac{4}{3}N\pi a^3$ ,  $\eta$  is the fluid viscosity, and  $\omega$  is the rotating frequency of the magnetic field (i.e., angular frequency of the sinusoidal current).

By combination of eq 6 and eq 7, a modified Mason number  $R_T$ ,<sup>29</sup> i.e., a parameter to estimate the stability of a rotating particle chain, is proposed, which can be expressed as

$$R_T = T_{\text{drag}} / T_{\text{mag}} \quad (8)$$

When  $R_T \leq 1$ , the induced magnetic torque is stronger than (or equal to) the viscous drag torque, maintaining the rotating chains stable. When  $R_T$  grows larger than 1, the magnetic torques are not able to counterbalance with the drag torque, and thus, the particle chains will be disassembled.

Through solving eq 8, the relationship between applied field parameters (i.e., applied field strength, and rotating frequency) and the stable length of particle chains can be obtained, the phase lag between  $T_{\text{drag}}$  and  $T_{\text{mag}}$  equals

$$\sin(2\alpha) = \frac{16\mu_0^3 (\mu + 2\mu_0)^2}{27(\mu - \mu_0)^2} \frac{N\eta\omega}{\mathbf{B}^2 \ln(\frac{N}{2})} \quad (9)$$

After the chains are formed, they rotate within the rotatory magnetic field with the defined phase lag  $\alpha$ , and because of the induced attractive interaction, the chains will synchronize with each other to form a large circular swarm with the diameter of  $D$ .

$$D = \pi N_C \left(\frac{L}{2}\right)^2 \quad (10)$$

where  $N_C$  is the number of particle chains, depending on the concentration of the nanoparticles of the local area, and  $L = 2Na$ , where  $a$  is the radius of a particle and  $N$  is the particle number from eq 9.

With the magnetic field model in eq 4 and swarm dynamics model in eq 9, a pH-dye-coated swarm in PBS buffer on the coverslip was formed and its size and position were controlled. The swarm size was defined through controlling the current in each of the coils from 0.2 to 8 A (peak-to-peak value of the sinusoidal current). Corresponding to these current magnitudes, the model-calculated swarm sizes were 0.5  $\mu\text{m}$  (for 0.2 A) and 50  $\mu\text{m}$  (8 A). The size of the experimentally generated

swarm ranged from  $0.52 \pm 0.15$  to  $52.7 \pm 2.6$   $\mu\text{m}$  ( $n = 5$  independent experiments), with the difference compared with model calculations less than 7.5% [Figure 2d]. The slight difference between the model-calculated swarm size and the experimentally formed swarm size can be attributed to the assumption in the model that the pole tips are perfectly sharp to a point and have no thickness whereas in experiments the pole tips had a finite radius and thickness. The system was not able to form a swarm smaller than 0.52  $\mu\text{m}$  because of its inability to generate a region with  $\mathbf{B}$  value larger than the value calculated in eq 9 for smaller swarms and because of the nonspecific aggregation of nanoparticles formed through van der Waals interactions. However, swarms larger than 52  $\mu\text{m}$  cannot be formed because the integrity of longer nanoparticle chains was broken by fluidic shear stress during chain rotation. When the size of the magnetic particle chain increases (i.e., particle number  $N$  increases) with the increased magnetic field flux density  $\mathbf{B}$ , the magnetic torque also increases [eq 5]. The fluid torque that balances the rotation of a chain also increases [eq 7], leading to a higher fluidic shear exerted on the particles. When the particle–particle interaction cannot withstand the fluidic shear, the nanoparticle chain is broken. Compared with magnetic swarms generated by Helmholtz coils,<sup>31,32</sup> the highly focused magnetic field created by our five-pole magnetic device is capable of generating a swarm that is smaller by at least an order of magnitude. The swarm's small size (e.g., 1  $\mu\text{m}$ ) is essential for performing measurements at precise locations in the intracellular environment.

To quantify the performance of swarm position control, trajectory tracking using a small swarm (1  $\mu\text{m}$ ) and a large swarm (25  $\mu\text{m}$ ) was performed [Figure 2e, Supplementary Video S2]. The average positioning error was 0.76  $\mu\text{m}$ , which was mainly because of thermal disturbance/Brownian motion. The maximum speed of the 1  $\mu\text{m}$  swarm was 18.4  $\mu\text{m/s}$  and was 5.2  $\mu\text{m/s}$  for the 25  $\mu\text{m}$  swarm. When exceeding the maximum speed, the swarm cannot maintain its integrity because of large fluidic shear to swarm boundary.

**Comparison with Single-Pole Magnetic Tweezers.** To compare the single-pole magnetic tweezers and the multiple magnetic tweezers in terms of swarm size control and swarm signal-to-noise ratio, we performed tests with single-pole magnetic tweezers by applying current to the movable pole only. The distance between the pole tip and the target position was adjusted from 50 to 200  $\mu\text{m}$ , and the current supplied in the coil was adjusted from 0.1 to 2 A. The one-directional attractive force produced by the single-pole magnetic tweezers generated particle chains toward the pole tip, and the chains had a significantly lower SNR than the swarms formed by the five-pole magnetic system, for instance, for a 25  $\mu\text{m}$  swarm [Figure 2f],  $13.22 \pm 4.19$  SNR vs  $27.5 \pm 1.36$  SNR ( $P$  value = 0.0002;  $n = 5$  independent swarms for each group) [Figure S4a]. The packing density of the swarm formed by single-pole magnetic tweezers was much lower than that by the five-pole magnetic tweezers. In terms of swarm size, with the 21.23  $\mu\text{m}$  movable pole tip in our system, the smallest swarm formed by the single-pole magnetic tweezers was  $13.61 \pm 1.76$   $\mu\text{m}$  [Figure S4b] whereas the five-pole device was capable of forming a swarm as small as 0.52  $\mu\text{m}$ . For larger swarms generated by the single-pole magnetic tweezers, the signal-to-noise ratio did not increase with the size of the swarm [Figure S4c] because the nanoparticles were loosely packed with lower interparticle forces.

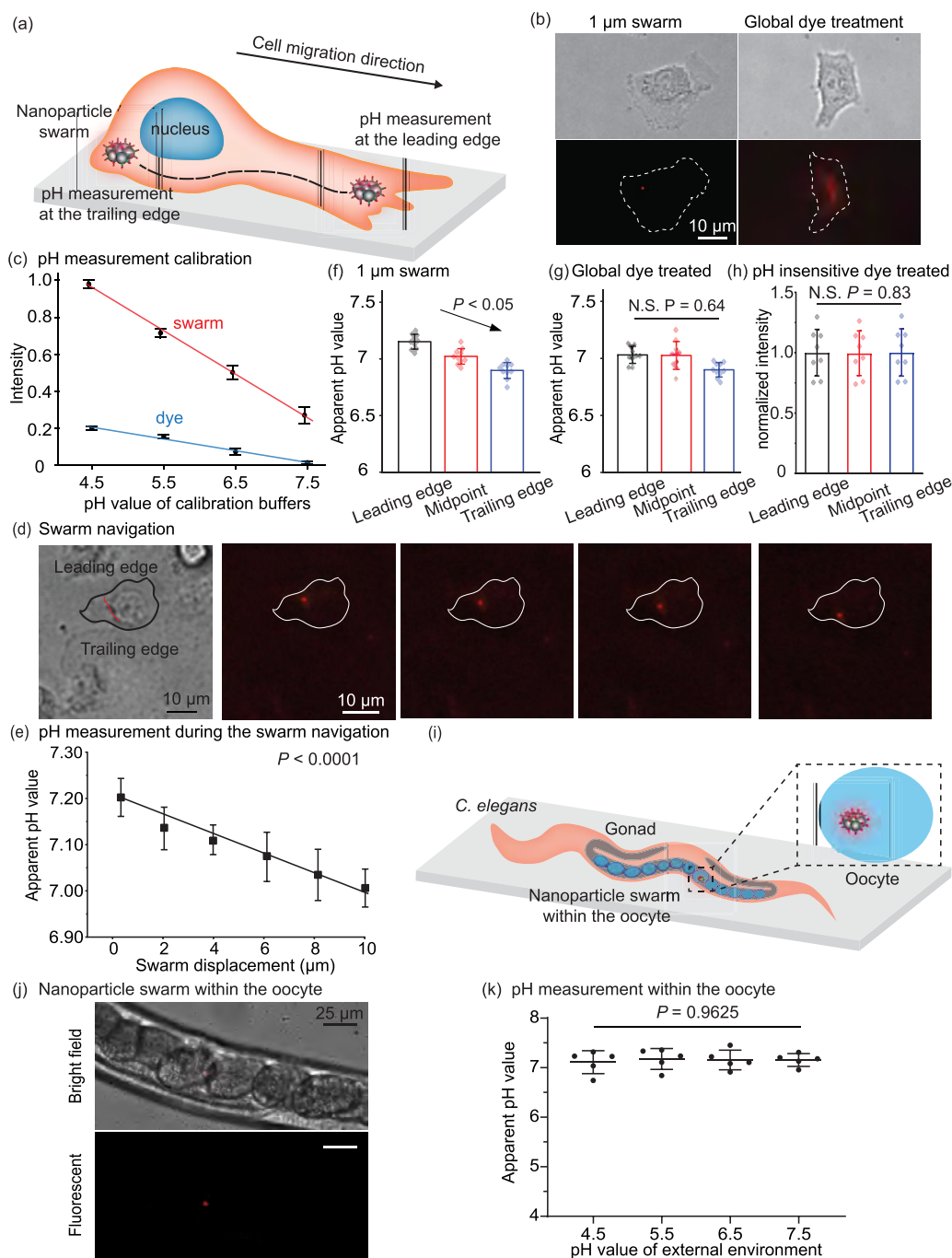


**Figure 3.** (a) Schematic of intracellular pH measurement in an intact cell using magnetic swarm. (b) pH measurement of a live cell using the 1  $\mu\text{m}$  swarm and using the global dye treatment. (c) pH calibration of the swarm and dye intensity within the cell using calibration buffers for different intracellular pH values. (d) Swarm motion trajectory. The motion trajectory was red highlighted. (e) Apparent pH measurement with the swarm displacement within the cell from the leading edge to the following edge.  $n = 10$  independently measured cells. (f) Apparent pH measurement in the same cell from the leading edge to the trailing edge using a 1  $\mu\text{m}$  swarm. Error bar: standard error.  $*P < 0.05$ ,  $n = 10$  independently measured cells. (g) Apparent pH measurement in the same cell from the leading edge to the trailing edge using global dye treatment. Error bar: standard error.  $*P < 0.05$ ,  $n = 10$  independently measured cells. (h) Measurement in the same cell using pH-insensitive dye Alexa 555-dye-coated nanoparticle swarm showed no significant difference in intensity measured from leading ledge to the trailing edge. Error bar: standard error.  $P = 0.83$ ,  $n = 10$  independently measured cells. (i) Schematic of intracellular pH measurement in an oocyte of a living *C. elegans* using magnetic swarm. (j) pH measurement within the oocyte using the nanoparticle swarm. (k) Apparent pH measurement within the oocytes showed the intraoocyte pH does not change with the pH change of the external environment. Error bar: standard deviation. One-way ANOVA  $P = 0.9625$ ,  $n = 5$  independently measured worms.

**Signal-to-Noise Ratio Calibration of Nanoparticle Swarm.** The pH-dye-coated magnetic nanoparticles were distributed evenly in the pH calibration buffer (pH = 4.5). The SNR was first measured before the magnetic field was applied.

This SNR quantified the effects from individual nanoparticles and nonspecific aggregation of nanoparticles. The system was then controlled to form swarms of different sizes [Figure 2g] and quantified the SNR for each swarm size. As summarized in

Figure 2h, the swarms increased SNR approximately 10 times compared with individual 130 nm particles (i.e., before magnetic field was applied). The fluorescent signal readout was almost constant for swarms larger than 1  $\mu\text{m}$  until 10  $\mu\text{m}$ , and for larger aggregates the packing density became slightly lower, which led to a slight decrease in SNR.

The SNR of the global dye treatment group can be enhanced by increasing dye concentration. However, a higher dye concentration causes more severe toxicity to cells. To compare the cytotoxicities between the global dye treatment group and the group of fluorescent-dye-coated magnetic nanoparticles, we increased pH dye concentration by 10 times from 20 to 200  $\mu\text{g}/\text{mL}$  for the global treatment group to achieve the same SNR by pH magnetic swarms. As shown in Figure 2i,j and Figure S5, cell viability (percentage of live cells on cell counting chips after being treated with Trypan Blue) in the global dye treatment group was significantly lower than that of the fluorescent-dye-coated magnetic nanoparticles group. These results established that for achieving the same SNR, cytotoxicity was lower by the magnetic swarm method than by the traditional global dye treatment approach.

#### Impact of Magnetic Swarm on Cellular Metabolism.

To understand how magnetic swarms impact cellular metabolism, mitochondria functions were assessed by measuring the oxygen consumption rate (OCR) and extracellular acidification rate (ECAR) of the cells. Cells in the treatment group were microinjected with nanoparticles, after which a 1  $\mu\text{m}$  swarm was formed in the cell and the swarm was navigated via position control for 20 min. The Seahorse assay was then performed to measure cell metabolism [Figure 2k] to determine basal respiratory, ATP-linked respiratory, non-mitochondrial respiratory, maximum respiratory capacity, and reverse capacity. We detected no difference in OCR and ECAR between the control group and the treatment group (Figure 2l: OCR,  $P = 0.8212$ ; ECAR,  $P = 0.3221$ ;  $n = 4$  independently repeated experiments), indicating that cellular metabolism was not overtly impacted by the intracellular swarms.

**Intracellular pH Measurement in Migrating Cells.** Cell migration involves precise coordination of cell protrusion and adhesion to the matrix at the leading edge and cell retraction and detachment from the matrix at the trailing edge.<sup>48</sup> The localization of proteins and regulators of the migratory machinery to either the cell front or its rear results in a spatial asymmetry, enabling cells to simultaneously coordinate cell protrusion and retraction.<sup>49</sup> Protons function as such unevenly distributed regulators by modulating the interaction of focal adhesion proteins and components of the cytoskeleton.<sup>50</sup> Intracellular pH gradient, caused by the proton distribution, appeared to be a prerequisite for cell migration.<sup>51</sup> Quantifying intracellular pH along the cell's migration direction [Figure 3a] can help understand cell directional motility, especially the migration of cancer cells.<sup>52</sup> The current global dye treatment method suffers from low SNR for quantifying pH distribution in live cells,<sup>50</sup> which is shown in Figure 3b. Hence, migrating cells are fixed and stained for increased SNR, but only an end-point measurement can be made and the dynamic changes during cell migration cannot be deciphered.<sup>53</sup>

After the pH-insensitive-dye-coated magnetic nanoparticles were delivered into cells (T24, human bladder cancer cell) via microinjection, according to eq 9 and eq 10, they were controlled to form a 1  $\mu\text{m}$  swarm inside the cell by applying a sinusoidal current with a magnitude of 1.02 A [Supplementary Video S3]. The size of the intracellular swarm reached

equilibrium in  $\sim 60$  s [Figure S6] and was  $0.96 \pm 0.17 \mu\text{m}$  ( $n = 10$  cells) in diameter. The size of the formed swarm was validated by scanning electron microscopy [Figure S7]. For calibration, the fluorescent intensity of 1  $\mu\text{m}$  swarms formed from the same pH-sensitive-dye-coated nanoparticles was calibrated by using intracellular pH calibration buffers with pH = 4.5, 5.5, 6.5, 7.5. The intracellular pH calibration buffer was first diluted into the loading solution with standard pH values. The cells were washed with Live Cell Imaging Solution and then incubated with the loading solution for 10 min. Then the intensity of the nanoparticle swarm was quantified. Because of the complex intracellular environment with different ionic strengths, the apparent pH value was used in experiments. Meanwhile, the intensity of the same amount of pH fluorescent dye in the same concentration as used for coating magnetic nanoparticles was measured [Figure 3c], which in essence is the global dye treatment method. The higher intensity of signal readout and lower background intensity contributed to the higher SNR of the magnetic swarms, resulting in a higher pH measurement sensitivity.

The swarm formed in the cell was then mobilized by the multipole magnetic tweezers from the leading edge to the trailing edge [Figure 3d, Supplementary Video S4, Figure S8]. On the basis of the calibration curve [Figure 3c], the fluorescent intensity of the swarm was used to quantify local pH along the swarm's trajectory [Figure 3e]. The positioning error of the swarm inside the cell was  $1.23 \pm 0.43 \mu\text{m}$ . Compared with the 0.76  $\mu\text{m}$  error in PBS, the larger positioning error inside the cell was likely because of the complex cytoplasmic network and the interactions of the magnetic swarm with cytoskeletal filaments. The electrical current supplied to each coil was kept at 1.02 A for maintaining the 1  $\mu\text{m}$  swarm, and the speed of the movable pole was controlled to be lower than 5  $\mu\text{m}/\text{s}$ . As quantified in the in vitro navigation experiments, this speed was proven not to cause the disassembly of the swarm under fluidic shear. The stability of the magnetic swarm in cells during navigation was quantified through moving a swarm of ion-insensitive nanoparticles (Alexa 555-coated nanoparticle swarm) within the cell while recording its intensity. The results showed an insignificant change in swarm intensity during navigation ( $P = 0.1782$ ,  $n = 7$  independent intracellular swarms, only one swarm was formed in each cell), proving stability of the swarms was well maintained [Figure S8].

The data summarized in Figure 3f reveal that pH consistently decreased along the magnetic swarm's trajectory from the leading edge, to the trajectory midpoint, and finally to the trailing edge ( $7.15 \pm 0.065$  vs  $7.02 \pm 0.068$  vs  $6.90 \pm 0.070$ ,  $n = 10$  cells). The  $t$  test trend analysis showed a significant trend ( $P = 0.008 < 0.01$ ) with a gradient of  $0.012 \pm 0.002$  pH change per micrometer in live cells. For comparison, cells were also globally treated with fluorescent dye in the same concentration as used for coating the magnetic nanoparticles. As shown in Figure 3g, no significant trend in fluorescent intensity from the leading edge to the trailing edge was found (trend analysis  $P = 0.32$ ). The results from global dye treatment showed that apparent pH values at the leading edge and at the trailing edge were different; however, the low SNR/sensitivity led to large measurement uncertainties and failed to reveal the gradient in apparent pH. Compared with the global dye treatment method, our magnetic swarm method used a lower amount of dye by  $8.5 \times 10^3$  times, yet achieved a much higher SNR. The results quantitatively revealed the gradient in

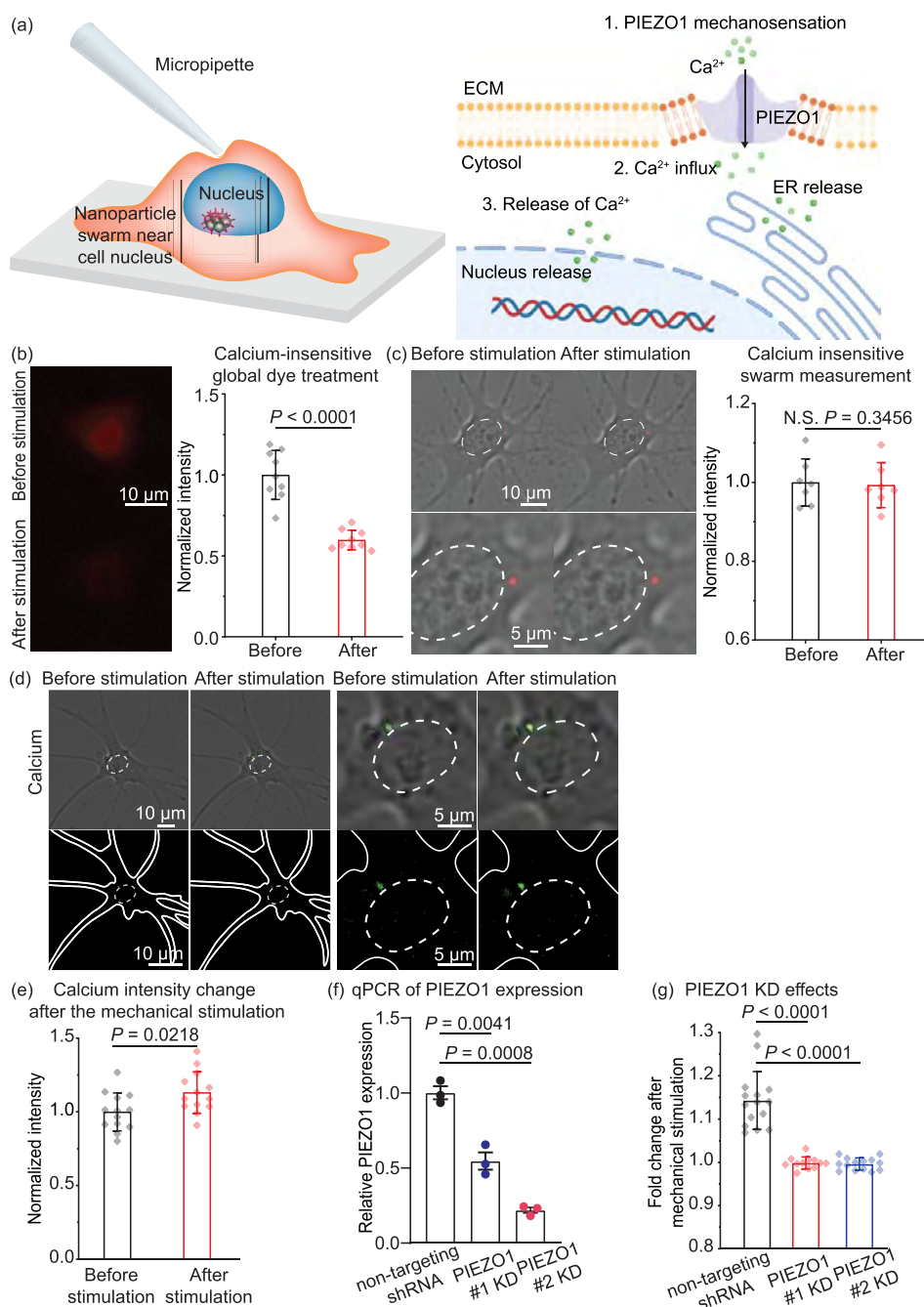


**Figure 4.** (a) Mechanical stimulation applied to the cell using a micropipette and the schematic of PIEZO1 mechanosensation and triggered calcium release. (b), (c) Cells treated with a calcium-insensitive dye (b) and with a calcium-insensitive-dye-coated nanoparticle swarm (c). (d) Calcium signal measured in the perinuclear region by an intracellular swarm before and after mechanical stimulation. Error bar: standard deviation.  $*P < 0.05$ ,  $n = 13$  independently measured cells. (e) Calcium signal fold change measured by a calcium-sensitive-dye-coated nanoparticle swarm and by a calcium-insensitive-dye-coated nanoparticle swarm in response to mechanical stimulation. Error bar: standard deviation.  $*P < 0.05$ ,  $n = 10$  independently measured cells. (f) Real-time quantitative PCR proving the successful knock-down of PIEZO1 protein in both PIEZO1 #1 and PIEZO1 #2 groups. Two knock-down groups using different RNA sequences were used to avoid off-target effects, and the control group was treated with scrambled control RNA. Error bar: standard deviation.  $*P < 0.05$ ,  $n = 3$  independently measured cells. (g) Fold change of the calcium signal at the perinuclear region after mechanical stimulation. Error bar: standard deviation.  $*P < 0.05$ ,  $n = 14$  independently measured cells.

apparent pH values and proved the existence of a polarized distribution of intracellular pH in a live migrating cell.

Negative control experiments using the 1  $\mu\text{m}$  swarm formed by pH-sensitive-dye-coated nanoparticles showed no significant changes in pH values within the leading or trailing edge [Figure 3h, Figure S9, leading edge:  $P = 0.8922$ , trailing edge:  $P = 0.8121$ ]. To further validate the results measured by the

swarm, fixation and staining experiments were performed. The results measured from the intensity of the fluorescent swarm were compared with those from the fluorescent dye signals measured from fixed cells. In fixed cells, the results showed a similar gradient [Figure S10].

To demonstrate the in vivo application of the swarm technique, we introduced pH-sensitive-dye-coated magnetic

nanoparticles into an oocyte within the free-living transparent nematode *C. elegans* [Figure 3i]. Living in the soil environment, *C. elegans* is naturally subject to environmental pH changes.<sup>54</sup> Measuring pH in the worm's reproductive cell can help understand how environmental changes such as soil acidification affect the model organism's development.<sup>55</sup>

Magnetic nanoparticles were microinjected into the distal gonad of adult *C. elegans* [Figure S11] via a standard *C. elegans* immobilization technique for nanoparticle injection.<sup>56</sup> Because the gonadal cytoplasm is continually packaged into maturing oocytes, a fraction of the injected beads were incorporated into the oocytes.<sup>57</sup> During injection, the worms were immobilized on a 2% agarose pad. The injected worms were transferred back to the nematode growth medium (NGM) plates and incubated at 22 °C for 2–6 h before being immersed into pH buffers of varying pH values. After a 75 min incubation in the pH buffer,<sup>58</sup> the worm was transferred to our five-pole magnetic tweezers system. A swarm was formed within the oocyte and its intensity was measured to quantify the intraoocyte pH value [Figure 3j]. The intraoocyte pH values were measured to be  $7.11 \pm 0.23$ ,  $7.17 \pm 0.21$ ,  $7.16 \pm 0.20$ , and  $7.16 \pm 0.13$  when the environmental pH changed from 4.5 to 5.5, 6.5, and 7.5 [Figure 3k,  $n = 5$  worms for each condition]. To quantify worm viability after the procedure, 20 additional worms were immobilized independently. Then we performed nanoparticle injection, formed a magnetic swarm, and performed pH measurement. The worms were then placed back on the nematode growth medium plates. Among the 20 worms, 19 of them restored their crawling behavior.

The tested range is the typical pH range of soil conditions that *C. elegans* experience, within which the oocyte was able to maintain a stable pH value, possibly because of the buffering effect from the voltage-gated ion channels. It was shown that the CLH-1 channel regulates intracellular pH via  $\text{HCO}_3^-$  flux.<sup>59</sup> Transcriptome analysis in an acidic environment showed upregulation of the *col*, *nas*, and *dpy* genes, which are required for cuticle synthesis and structure integrity.<sup>60</sup> Although our data showed that the *C. elegans* was able to maintain pH in the oocyte within the environmental pH range 4.5–7.5, the growth and reproduction processes of *C. elegans* might be affected in a more severe acidic environment, which requires further investigation.

**Increase of Calcium at the Perinuclear Region in Response to Mechanical Stimulation.** Calcium signaling is essential for cell proliferation,<sup>61–65</sup> gene transcription,<sup>66–70</sup> and cell death,<sup>71–73</sup> and was also recently shown to regulate mechanosensation in cancer cells.<sup>74,75</sup> Substantial research has established the connection of nuclear calcium to a wide range of physiological and pathological responses of cells.<sup>76</sup> Although nuclear calcium is essential for processes such as nuclear transport, chromatin condensation, and the activation of several transcription factors, the origin of nuclear calcium signaling in response to mechanical stimulation remains elusive.<sup>77,78</sup>

The perinuclear region, defined as the surrounding cytoplasmic region of the nucleus, is at the traffic center for material exchange between the cytoplasm and nucleoplasm. Understanding the calcium change at the perinuclear region would help better understand the source of the nuclear calcium. Calcium staining in fixed cells showed a ring with higher intensity surrounding the cell nucleus, indicating a higher free calcium concentration in the perinuclear regions than in the nuclear centers in the initial state of the cell.<sup>77</sup>

Upon mechanical stimulation, the nuclear calcium increases follow a cytosolic calcium increase with a short delay, and this delay was hypothesized to be likely because of the calcium diffusion from the perinuclear region through the nuclear pores.<sup>79</sup> To understand the calcium signal at the perinuclear region when it is subject to mechanical stimulation on the cell membrane, we used the swarm technique to quantify calcium signal changes in a site-specific manner at the perinuclear region before and after mechanical stimulation. With recent studies showing growing knowledge on the mechanical response of tumors,<sup>80</sup> the glioblastoma stem cell G532 was used as the model in this study.

When mechanical stimulation is applied on the cell membrane [Figure 4a], in the traditional global dye treatment method, cell deformation can artificially alter the local dye concentration and fluorescent signal readout. This bias poses challenges to precisely measure mechanical stimulation-induced intracellular calcium changes. To quantify such a bias, we used Alexa 555 dye, which is insensitive to intracellular calcium concentration change, to globally treat cells. We then applied mechanical stimulation by using a micropipet to indent the cell (above the center of the cell nucleus) by  $2 \mu\text{m}$ . The cell deformation from micropipet indentation caused the Alexa 555 signal to change significantly [Figure 4b and Supplementary Video S5]. We investigated whether such a signal bias occurs to a swarm of Alexa 555-dye-coated magnetic nanoparticles. With the models in eq 4 and eq 10, a  $1 \mu\text{m}$  swarm was formed at the perinuclear region in the cell [Figure 4c]. When the same  $2 \mu\text{m}$  mechanical indentation was applied, interestingly, the signal of the calcium insensitive Alexa 555-dye-coated swarm did not significantly change [Figure 4c], showing that the swarm's signal was not sensitive to the cell deformation caused by mechanical stimulation.

For calibration, the fluorescent intensity of the  $1 \mu\text{m}$  calcium-dye-coated swarm was measured by using calcium calibration buffers with a concentration of 0.017, 0.038, 0.065, 0.100, 0.225, and  $0.602 \mu\text{M}$ . The intensity of the same amount of calcium fluorescent dye in the same concentration as used for coating magnetic nanoparticles was also measured [Figure S12]. The results showed that the  $1 \mu\text{m}$  swarm of calcium-dye-coated nanoparticles increased the SNR significantly ( $P < 0.0001$ ), compared to results from the global dye treatment. The fold increase was not as large as for the pH dye because different types of dye result in different sizes of functionalized nanoparticles and thus various local concentration effects in a swarm. SEM imaging revealed that the pH-dye-coated nanoparticles were significantly smaller than the calcium-dye-coated nanoparticles ( $153.5 \pm 12.6 \text{ nm}$  vs  $226.9 \pm 14.7 \text{ nm}$ ,  $P < 0.0001$ ,  $n = 50$  nanoparticles).

The swarms were used to measure intracellular calcium concentration changes at the perinuclear region in response to mechanical stimulation. A micropipet controlled by a micro-manipulator was used to generate a local cell deformation of  $2 \mu\text{m}$  (above the cell center) whereas the calcium signal was measured at the perinuclear region [Figure 4d,e]. The measurement results revealed a significant calcium signal change at the perinuclear region in response to mechanical stimulation ( $1.00 \pm 0.13$  vs  $1.13 \pm 0.14$ ,  $P = 0.0218$ ,  $n = 13$  independent cells) [Figure 4e, Supplementary Video S6]. The PIEZO transmembrane proteins are evolutionarily conserved ion channels that are intrinsically mechanosensitive.<sup>75</sup> As schematically shown in Figure 4a, mechanical stimulation was hypothesized to trigger the opening of the PIEZO1 channel,

which causes an influx of calcium and then the release of intracellular calcium stored in the endoplasmic reticulum (ER) and the release by the cell nucleus into the cytoplasm [Figure 4a] after mechanical stimulation was applied on the cell membrane and transmitted to nuclear envelope through the cytoskeleton.<sup>81–83</sup> Therefore, we used shRNA (Methods) to knock down the mechano-sensitive ion channel PIEZO1. Effective knock-down was validated by using real-time quantitative PCR [Figure 4g]. Two knock-down groups were included to avoid off-target effects. Compared with the control group, the knock-down groups showed a significantly lower calcium signal difference before and after mechanical stimulation (fold change in the control,  $1.143 \pm 0.067$ ; fold change in knock-down group #1,  $0.998 \pm 0.014$ ; fold change in knock-down group #2,  $0.996 \pm 0.014$ ;  $P < 0.05$ ,  $n = 14$  cells) [Figure 4f, Figure S13]. These results provided evidence that such a mechanical stimulation-induced perinuclear calcium level increase depends on the PIEZO1 function. The PIEZO1-dependent calcium release can likely be attributed to the calcium release from the ER, which stores the majority of intracellular calcium.<sup>84</sup> The perinuclear region is at the traffic center for material exchange between the cytoplasm and nucleoplasm. Further investigations will be made on whether the increase of the perinuclear calcium increase causes a higher transportation of the calcium into the nucleus and affects epigenetic changes.

## CONCLUSION

Intracellular measurement is critical for studying cell signaling and identifying therapeutic targets for disease treatment.<sup>85</sup> Traditional global dye treatment suffers from low SNR, and improving SNR by increasing dye concentration causes higher toxicity to cells. Using microrobotic swarms of fluorescent-dye-coated magnetic nanoparticles, we showed that local dye concentration was accurately controlled, and SNR was increased without sacrificing cell viability. In existing magnetic micromanipulation systems, the generated swarms ranged from tens of micrometers<sup>30,31</sup> to several hundreds of micrometers,<sup>32,33</sup> which are not suitable for performing intracellular measurement. In swarm position control, existing techniques utilized the rotating magnetic field to roll the swarm along the substrate;<sup>29</sup> however, the substrate of the intracellular environment with cytoskeleton and intracellular organelles can impede the motion and cause the swarm to lose stability. Differently, our system with a movable pole and four stationary poles generates a gradient field, with a local maximum field strength on the 2D plane to control the swarm position by controlling the position of the local maximum field strength. Stability of the swarm was well maintained inside the cell, and the results showed no significant intensity change during swarm navigation [Figure S8]. The size of the generated swarms was accurately controlled (from 0.52 to 52.7  $\mu\text{m}$  with an error less than 7.5%), and the position of a 1  $\mu\text{m}$  swarm was controlled with a positioning accuracy of 0.76  $\mu\text{m}$ , through controlling the current and movable pole position of the multipole magnetic tweezers device using our proposed models.

The experiments of intracellular pH measurement using a 1  $\mu\text{m}$  swarm revealed the polarized apparent pH distribution in migrating cells. The intracellular apparent pH measurement was also performed inside the oocyte of living *C. elegans*. The intracellular calcium measurement made with 1  $\mu\text{m}$  swarms quantified calcium changes at the perinuclear region before and

after mechanical stimulation, whereas the traditional calcium dye approach cannot provide a site-specific measurement.

The avidin–biotin complex is one of the strongest known noncovalent interactions between a protein and ligand.<sup>86</sup> The bond formation between biotin and avidin is rapid, and once formed, is not affected by pH, temperature, organic solvents and other denaturing agents.<sup>87</sup> Thus, we chose the avidin–biotin interaction for functionalizing the fluorescent sensor onto the nanoparticle surface. As shown in Figure S1, two strategies (using either an avidin nanoparticle or a biotin nanoparticle) were adopted for coating the nanoparticle, rendering the protocol applicable to the intracellular measurement of a broad range of ions such as potassium and sodium. If the fluorescent sensor is unavailable in biotin form (to be coated with an avidin nanoparticle), the avidin-formed sensor (to be coated with a biotin nanoparticle) can also be used in the proposed technique. In addition to functionalization with a specific type of fluorescent sensor, our technique bears the potential for multiple channel measurement through forming a swarm of nanoparticles with different surface functionalizations. For instance, temperature-sensitive-dye-coated nanoparticles and pH-dye-coated nanoparticles can be used together to form swarms for simultaneous measurement of pH and temperature. Future work can investigate the intracellular synthesis of magnetic nanoparticles as inspired by ref 18 and colabel with fluorescent ion sensors.<sup>88</sup> Such in situ capability can further improve the biocompatibility of nanoparticles and also circumvent the need for nanoparticle delivery.

The swarm of nanoparticles provides a promising avenue for simultaneous mechanical stimulation and ion concentration quantification inside a cell. The generated swarm can be manipulated by using the multipole magnetic tweezers to apply mechanical force onto intracellular organelles (e.g., cell nucleus or endoplasmic reticulum) while monitoring the ion concentration with the same swarm. This simultaneous stimulation and measurement approach would enable the pursuit of such questions as whether physical force directly applied to the endoplasmic reticulum can generate calcium release and subsequent biochemical cascades.

A potential limitation of our technique is its present incapability for temporally spatially stringent measurements. For instance, in our intracellular pH measurement, the navigation of the swarm from the leading edge to the trailing edge ( $\sim 20 \mu\text{m}$  in distance) took approximately 60 s. This long travel time was acceptable for measuring the pH gradient in the cell polarization state because the time scale of cell polarization during cell migration is in hours,<sup>89,90</sup> however, for measuring fast dynamic behaviors in the subsecond time scale and in different intracellular locations, positioning of our microrobotic swarm would not be fast enough.

## METHODS

**Device Fabrication and Assembly.** The five-pole magnetic tweezers consist of four stationary magnetic poles made of high-permeability foils (Silicon Iron Alloys, MuShield, USA), a movable pole made from iron rod, a magnetic yoke connecting the four foil poles, and four magnetic coils. The four stationary poles were fabricated through electric discharge machining, achieving a small tip radius around 1.4  $\mu\text{m}$ . The four stationary magnetic poles were assembled for 400  $\mu\text{m}$  between each pair, to leave sufficient workspace for cell imaging. The movable pole was fabricated by a lathe. The magnetic yoke was fabricated through CNC machining with a tolerance of 0.1 mm. Coils (Magnetic Wire, Gauge 14,

Digikey) were wired onto the cores on the yoke and on the movable pole. The four stationary poles were assembled onto an ylic plate with alignment marks engraved by laser machining under a microscope to ensure the alignment of each pole pairs. The movable pole was fixed onto a three-axis manipulator. The relative positions of the tip of the movable pole and tips of the four stationary poles were adjusted under the microscope field of view.

**Cell Culture.** Human bladder cancer T24 cells were purchased from the America Type Culture Collection (ATCC, Manassas, VA). The cells were cultured with ATCC-formulated McCoy's 5A modified medium with 10% FBS and 1% penicillin–streptomycin at 37 °C and 5% CO<sub>2</sub> and passaged every 4 days. Glioblastoma stem cells G532 were grown adherently in serum-free medium as described in ref 91. Briefly, cells were grown on PRIMARIATM culture plates (Corning) coated with poly-L-ornithine (Sigma) and laminin (Sigma) and maintained in Neurocult NS-A basal medium (human) (StemCell Technologies) containing 2 mM L-glutamine (Wisent), 75 μg/mL bovine serum albumin (Life Technologies), in-house hormone mix equivalent to N2 (homemade), B27 supplement (Life Technologies), 10 ng/mL recombinant human epidermal growth factor (rhEGF; Sigma), 10 ng/mL basic fibroblast growth factor (bFGF; StemCell Technologies), and 2 μg/mL heparin (Sigma). Cells were passaged by using enzymatic dissociation with Accutase (StemCell Technologies).

**Cell Viability Test.** Magnetic nanoparticles were added into the cell culture 12 h prior to cell viability counting, and fluorescent dyes were added into the cell culture 1 h prior to cell viability counting, following the manufacturer's protocol. In the cell-counting procedure, cells were first lifted by treating with 0.25% trypsin (0.25% trypsin, Sigma-Aldrich). The resulting cell suspension was centrifuged, and the cell pellet was resuspended in the cell medium to a final concentration of approximately  $1 \times 10^6$  cells/mL. A 1:1 mixture of cell suspension and 0.4% Trypan Blue solution (15250061, ThermoFisher Scientific) was then made and allowed to stand for 5 min at room temperature. For cell counting, a 10 μL of cell suspension was applied to the edge of the V-shaped groove in the chamber of a disposable hemocytometer (C-Chip disposable hemocytometer, Digital Bio). Cells were allowed to drop to the chamber bottom for 1–2 min before counting.

**Microinjection.** The microinjection system used in this work consisted of a standard inverted microscope (Nikon TE2000-S, Nikon Microscopes), a micromanipulator (MX7600, Siskiyou, Inc.), a picoliter pump (Digital Microinjector, Sutter Instrument USA), and a glass micropipet, which was laser pulled through heating a microfilament. A camera was connected to the microscope to provide microscopy imaging and visual feedback. A host computer runs our custom-built control software to control all the aforementioned instruments.<sup>92</sup> Microinjection was conducted (injection pressure 5.4 kPa, injection pipet inner diameter 900–1000 nm, injection pulse duration 0.2 s) to deliver 4 pL of nanoparticle solution with a concentration of 100 μg/mL. The intracellular amount of the nanoparticles was estimated to be ~140 particles per cell. Cell microinjection was performed with different sizes of magnetic nanoparticles (130, 250, 500, and 1000 nm), and the cell viability and the success rate of microinjection were compared. The microinjection of 130 nm nanoparticles (nanomag-D biotin, Micromod, Germany) showed insignificant cell viability decrease compared to results with the control group, and the highest microinjection success rate among all particle sizes tested.

**Preparation of Fluorescent-Dye-Coated Nanoparticles.** The pH sensitive fluorescent dye, pHrodo red avidin (P35362, ThermoFischer Scientific), was used for coating onto the surface of magnetic particles. The pHrodo red avidin construct in a concentration of 2 mg/mL and the biotin-coated magnetic particles in a concentration of 10 mg/mL were mixed in a ratio of 2:1 overnight at 4 °C. The coated magnetic particles were washed by 4 °C PBS three times with a volume ratio of particles solution:PBS = 1:1000. At the final working concentration of 100 μg/mL, the coated magnetic particles were examined under the microscope, and no observable aggregate larger than 200 nm was found. Cal-520 biotin conjugate (20605, ATT Bioquest, USA) was used to be integrated

onto the surface of avidin magnetic nanoparticles (nanomag-D avidin, Micromod, Germany). The coating procedures are similar to the pH dye functionalization, including mixing with particles overnight at 4 °C and washing with PBS at 4 °C before use. The final coating efficiency was quantified through the BCA assay [Figure S14]. The fluorescent intensity of the formed pH-sensitive and calcium-sensitive nanoparticle swarm was calibrated in the pH calibration buffer (Intracellular pH Calibration Buffer, ThermoFisher) and calcium calibration buffer (Calcium Calibration Buffer Kits, ThermoFisher), respectively. The pH-insensitive and calcium-insensitive nanoparticle swarm was also tested within the calibration buffers as negative control groups [Figure S15]. The dye treatment was also used in fixed cells to study the effects of the nanoparticle swarm to the measurement results [Figure S16].

**Lentivirus-Mediated shRNA for PIEZO1 Knock-Down.** The human pLKO.1 lentiviral shRNA target gene set against PIEZO1 and pLKO.1-TRC-control vector were obtained from Dharmacon. Virus infections were performed within antibiotics-free culture medium for 24 h. PIEZO1 shRNA mature antisense sequences: #, ATGATTGTACTTCTTGGTGAG; #2, TTCCACCTGAATGTGGTCTTC. Cells were collected for RNA extraction after 4 days starting from lentiviral infections.

**Real-Time Quantitative PCR.** The total RNA from cells was isolated by using GENEzol TriRNA Pure Kit according to the manufacturer's protocol (GeneAld Biotech Ltd.). cDNAs were synthesized with the Tetro reverse transcriptase (Bioline). Real-time PCR was performed by using the following specific human primers: PIEZO1 (forward, CTCTTCCTGGCGCTGTTC; reverse, GATGAGGTTGGTGGAGTTGG); GAPDH (forward, CTCCTGCACCACTGCT; reverse, GGGCCATCCACAGTCTTCTG). GAPDH was used as internal controls for gene expression quantification. Real-time PCR was performed with ABI Viiia7 by using SYBR green PCR master mix. Relative mRNA abundance was done using the  $\Delta\Delta CT$  method (in triplicates). Each experiment was performed in three biological replicates.

**Fluorescent Staining.** Cell nucleus staining in live cells was achieved by using Hoechst (62249, Hoechst solution, ThermoFisher Scientific). Hoechst was diluted in the stock solution of DMSO to reach a final concentration of 1 mg/mL. Dye in stock solution was added into the cell culture medium to reach the final concentration of 1 μg/mL, and the cells were treated at 37 °C for 40 min. Then the dye was washed by PBS three times. Intracellular organelles were stained by using Organelle Localization IF Antibody Sampler Kit (#8653, Cell Signaling Technology, USA) as the primary antibody with a dilution ratio following manufacturer protocol and antimouse secondary antibody (715-095-151, 1:500, Donkey anti-Mouse IgG (H+L) Secondary Antibody, FITC, Jackson Immuno research) as the secondary antibody. Staining for actin was achieved by using phalloidin fluorescent conjugate (ab176756, Phalloidin-iFluor 555, 1:2000, Abcam). Cells were fixed, permeabilized, treated with primary antibody, secondary antibody, and mounted in DAPI (H1200 Vectashield+DAPI, VectorLabs) as manufacturer protocols instructed to visualize the nucleus.

**Fluorescence Imaging.** The intracellular navigation and measurement experiments were conducted while images/videos were collected through a Nikon epifluorescent microscope (Eclipse Ti2) with illumination light sources (Lumencor, USA). The images and videos were acquired by a Hamamatsu ORCA-Flash4 camera connected to the microscope with 40× objective. The imaging settings for pH calibration and measurement include the following: excitation filter, 504 nm; barrier filter, 609 nm; exposure time, 200 ms. The imaging settings for calcium measurement include the following: excitation filter, 466 nm; barrier filter, 525 nm; exposure time, 200 ms.

**Data Analysis for Fluorescent Intensity.** Cell experiments were completed within 30 min after cells were taken out of incubator, with each trail of experiments completed within 5 min. The intensity of fluorescent signal was analyzed by ImageJ and MATLAB 2020a. The photobleaching effect was experimentally calibrated [Figure S16] and used to correct the recorded intensity results. The rolling ball filtering algorithm was applied to the fluorescence images.<sup>93</sup> The size of the

formed 1  $\mu\text{m}$  swarm was quantified to be  $1.037 \pm 0.037 \mu\text{m}$  after filtering the fluorescence images and  $1.036 \pm 0.026 \mu\text{m}$  measured by transmission electron microscopy. There was no significant difference in the swarm size between the results determined from TEM images and the filtered fluorescence images ( $P = 0.9561$ ). The analysis code is available at <https://github.com/XianShawn/IntracellularSwarm>.

**Error Propagation.** Because of measurement uncertainties in calibration and the variance in different cells, the apparent pH/calcium values calculated from experimental data contain uncertainties from both calibration and experiments. The calibration data were first fitted with the weighted linear least-squares regression model. The weight for each  $y$  data point is  $\frac{1}{\sigma^2}$ , where  $\sigma$  is the standard deviation. With the weighted linear least-squares regression model, the uncertainty in the estimation was calculated as

$\sigma_{\text{est}} = \sqrt{\frac{\sum(y_{\text{model}} - y_{\text{mean}})^2}{N}}$ , where  $y_{\text{model}}$  is the calibration-predicted value and  $y_{\text{mean}}$  is the experimentally measured value. The combined standard deviation is  $\sigma_{\text{total}} = \sqrt{\sigma_{\text{est}}^2 + \sigma_{\text{mean}}^2}$ , where  $\sigma_{\text{mean}}$  is the standard deviation of the experimentally measured mean value.

**Statistical Test.** The polarity ratio and the stiffening ratio were reported as mean  $\pm$  standard deviation. Comparisons of each group were conducted by one-way ANOVA and the Student–Newman–Keuls test for pairwise comparisons in Origin. The statistical significance in each comparison was evaluated as  $p < 0.05$  for significance level.

## ASSOCIATED CONTENT

### Supporting Information

The Supporting Information is available free of charge at <https://pubs.acs.org/doi/10.1021/acsnano.2c02938>.

Figure S1, nanoparticle functionalization based on avidin–biotin binding; Figure S2, five-pole magnetic tweezer system; Figure S3, magnetic field simulation with contours of the same field strength within the 3D space; Figure S4, signal-to-noise ratio of swarms formed by single-pole magnetic tweezers; Figure S5, Trypan Blue cell viability assay for cell viability; Figure S6, swarm formation time of swarms with different sizes; Figure S7, scanning electron microscope image of an intracellular swarm; Figure S8, stability of magnetic swarm during navigation within a cell; Figure S9, pH measurement within the same edge using magnetic swarm; Figure S10, pH measurement in fixed cells; Figure S11, microinjection of the nanoparticles into the living *C. elegans*; Figure S12, calcium fluorescent signal calibration; Figure S13, calcium measurement after knocking down PIEZO1; Figure S14, BCA assay for quantifying dye grafting density; Figure S15, negative control of non-calcium-sensitive-dye-coated nanoparticles; Figure S16, photobleaching curve of pH and calcium measurement (PDF)

Schematic of intracellular measurement using micro-robotic swarm (MP4)

Swarm position control of a small swarm and a large swarm (MP4)

Intracellular swarm formation within the cell (MP4)

Intracellular pH measurement inside a migrating cell (MP4)

Cells treated with Alexa 555 dye in response to mechanical stimulation (MP4)

Intracellular calcium measurement after mechanical stimulation (MP4)

## AUTHOR INFORMATION

### Corresponding Authors

**Changhai Ru** – School of Electronic and Information Engineering, Suzhou University of Science and Technology, Suzhou 215009, China; Email: [rchai@163.com](mailto:rchai@163.com)

**Xi Huang** – Program in Developmental and Stem Cell Biology and Arthur and Sonia Labatt Brain Tumour Research Centre, The Hospital for Sick Children, Toronto M5G 1X8, Canada; Department of Molecular Genetics, University of Toronto, Toronto, Ontario M5S 1A8, Canada; Email: [xi.huang@sickkids.ca](mailto:xi.huang@sickkids.ca)

**Yu Sun** – Department of Mechanical and Industrial Engineering, University of Toronto, Toronto M5S 3G8, Canada; Institute of Biomedical Engineering, University of Toronto, Toronto M5S 3G9, Canada; Department of Electrical and Computer Engineering and Department of Computer Science, University of Toronto, Toronto M5S 3G4, Canada; [orcid.org/0000-0001-7895-0741](https://orcid.org/0000-0001-7895-0741); Email: [yu.sun@utoronto.ca](mailto:yu.sun@utoronto.ca)

### Authors

**Xian Wang** – Department of Mechanical and Industrial Engineering, University of Toronto, Toronto M5S 3G8, Canada; Program in Developmental and Stem Cell Biology and Arthur and Sonia Labatt Brain Tumour Research Centre, The Hospital for Sick Children, Toronto M5G 1X8, Canada; [orcid.org/0000-0002-1501-2544](https://orcid.org/0000-0002-1501-2544)

**Tiancong Wang** – Department of Mechanical and Industrial Engineering, University of Toronto, Toronto M5S 3G8, Canada

**Xin Chen** – Program in Developmental and Stem Cell Biology and Arthur and Sonia Labatt Brain Tumour Research Centre, The Hospital for Sick Children, Toronto M5G 1X8, Canada; [orcid.org/0000-0001-7620-5975](https://orcid.org/0000-0001-7620-5975)

**Junhui Law** – Department of Mechanical and Industrial Engineering, University of Toronto, Toronto M5S 3G8, Canada; [orcid.org/0000-0002-6033-7639](https://orcid.org/0000-0002-6033-7639)

**Guanqiao Shan** – Department of Mechanical and Industrial Engineering, University of Toronto, Toronto M5S 3G8, Canada

**Wentian Tang** – Department of Mechanical and Industrial Engineering, University of Toronto, Toronto M5S 3G8, Canada; [orcid.org/0000-0003-1454-2022](https://orcid.org/0000-0003-1454-2022)

**Zheyuan Gong** – Department of Mechanical and Industrial Engineering, University of Toronto, Toronto M5S 3G8, Canada

**Peng Pan** – Department of Mechanical and Industrial Engineering, University of Toronto, Toronto M5S 3G8, Canada; Department of Mechanical Engineering, McGill University, Montreal H3A 0C3, Canada

**Xinyu Liu** – Department of Mechanical and Industrial Engineering, University of Toronto, Toronto M5S 3G8, Canada; Institute of Biomedical Engineering, University of Toronto, Toronto M5S 3G9, Canada

**Jiangfan Yu** – School of Science and Engineering, The Chinese University of Hong Kong, Shenzhen S18172, China; Shenzhen Institute of Artificial Intelligence and Robotics for Society (AIRS), Shenzhen S18172, China; [orcid.org/0000-0002-7981-6744](https://orcid.org/0000-0002-7981-6744)

Complete contact information is available at: <https://pubs.acs.org/doi/10.1021/acsnano.2c02938>

## Author Contributions

#X.W. and T.W. contributed to this work equally.

## Notes

The authors declare no competing financial interest. The data shown in this paper including all figures are available through GitHub at [https://github.com/XianShawn/intracellular\\_swarm](https://github.com/XianShawn/intracellular_swarm). The data are for the purpose of reproducible research and should not be used for commercial purposes.

## ACKNOWLEDGMENTS

The authors thank Z. Zhang and C. Dai for their helpful suggestions. This work was supported by the National Sciences and Engineering Research Council of Canada, by the Ontario Research Fund via the Research Excellence Program, and by the Canada Research Chairs Program.

## REFERENCES

- (1) Han, J.; Burgess, K. Fluorescent Indicators for Intracellular pH. *Chem. Rev.* **2010**, *110*, 2709–2728.
- (2) Yin, J.; Hu, Y.; Yoon, J. Fluorescent Probes and Bioimaging: Alkali Metals, Alkaline Earth Metals and pH. *Chem. Soc. Rev.* **2015**, *44*, 4619–4644.
- (3) Okabe, K.; Inada, N.; Gota, C.; Harada, Y.; Funatsu, T.; Uchiyama, S. Intracellular Temperature Mapping with a Fluorescent Polymeric Thermometer and Fluorescence Lifetime Imaging Microscopy. *Nat. Commun.* **2012**, *3*, 705.
- (4) Carter, K. P.; Young, A. M.; Palmer, A. E. Fluorescent Sensors for Measuring Metal Ions in Living Systems. *Chem. Rev.* **2014**, *114*, 4564–4601.
- (5) Sahl, S. J.; Hell, S. W.; Jakobs, S. Fluorescence Nanoscopy in Cell Biology. *Nat. Rev. Mol. Cell Biol.* **2017**, *18*, 685–701.
- (6) Yao, Z.; Carballido-López, R. Fluorescence Imaging for Bacterial Cell Biology: From Localization to Dynamics, from Ensembles to Single Molecules. *Annu. Rev. Microbiol.* **2014**, *68*, 459–476.
- (7) Pinaud, F.; Michalet, X.; Bentolila, L. A.; Tsay, J. M.; Doose, S.; Li, J. J.; Iyer, G.; Weiss, S. Advances in Fluorescence Imaging with Quantum Dot Bio-Probes. *Biomaterials* **2006**, *27*, 1679–1687.
- (8) Meyer, T.; Teruel, M. N. Fluorescence Imaging of Signaling Networks. *Trends Cell Biol.* **2003**, *13*, 101–106.
- (9) Moerner, W. E.; Fromm, D. P. Methods of Single-Molecule Fluorescence Spectroscopy and Microscopy. *Rev. Sci. Instrum.* **2003**, *74*, 3597–3619.
- (10) Icha, J.; Weber, M.; Waters, J. C.; Norden, C. Phototoxicity in Live Fluorescence Microscopy, and How to Avoid It. *BioEssays* **2017**, *39*, 1700003.
- (11) Yu, J.; Wang, Q.; Li, M.; Liu, C.; Wang, L.; Xu, T.; Zhang, L. Characterizing Nanoparticle Swarms with Tuneable Concentrations for Enhanced Imaging Contrast. *IEEE Robot. Autom. Lett.* **2019**, *4*, 2942–2949.
- (12) Jensen, E. C. Use of Fluorescent Probes: Their Effect on Cell Biology and Limitations. *Anat. Rec.* **2012**, *295*, 2031–2036.
- (13) Laissue, P. P.; Alghamdi, R. A.; Tomancak, P.; Reynaud, E. G.; Shroff, H. Assessing Phototoxicity in Live Fluorescence Imaging. *Nat. Methods* **2017**, *14*, 657–661.
- (14) Romana, B.; Hassan, M. M.; Sonvico, F.; Garrastazu Pereira, G.; Mason, A. F.; Thordarson, P.; Bremmell, K. E.; Barnes, T. J.; Prestidge, C. A. A Liposome-Micelle-Hybrid (LMH) Oral Delivery System for Poorly Water-Soluble Drugs: Enhancing Solubilisation and Intestinal Transport. *Eur. J. Pharm. Biopharm.* **2020**, *154*, 338–347.
- (15) Zhang, Y.; Huang, Y.; Li, S. Polymeric Micelles: Nanocarriers for Cancer-Targeted Drug Delivery. *AAPS PharmSciTech* **2014**, *15*, 862–871.
- (16) Zborowski, M.; Chalmers, J. J. *Magnetic Cell Separation*, 1st ed.; Elsevier: Amsterdam, 2008.
- (17) Monzel, C.; Vicario, C.; Piehler, J.; Coppey, M.; Dahan, M. Magnetic Control of Cellular Processes Using Biofunctional Nanoparticles. *Chem. Sci.* **2017**, *8*, 7330–7338.
- (18) Liße, D.; Monzel, C.; Vicario, C.; Manzi, J.; Maurin, I.; Coppey, M.; Piehler, J.; Dahan, M. Engineered Ferritin for Magnetogenetic Manipulation of Proteins and Organelles Inside Living Cells. *Adv. Mater.* **2017**, *29*, 1700189.
- (19) Wang, X.; Law, J.; Luo, M.; Gong, Z.; Yu, J.; Tang, W.; Zhang, Z.; Mei, X.; Huang, Z.; You, L.; Sun, Y. Magnetic Measurement and Stimulation of Cellular and Intracellular Structures. *ACS Nano* **2020**, *14*, 3805–3821.
- (20) Yurenaya, A. Yu.; Nikitin, A. A.; Gabbasov, R. R.; Polikarpov, M. A.; Cherepanov, V. M.; Chuev, M. A.; Abakumov, M. A.; Panchenko, V. Ya. Studying the Effect of Brownian Motion on the Mössbauer Spectra of Nanoparticles in a Medium Simulating Cell Cytoplasm. *Bull. Russ. Acad. Sci.: Phys.* **2020**, *84*, 1399–1402.
- (21) Kim, J.; Jeong, H.; Southard, K. M.; Jun, Y.; Cheon, J. Magnetic Nanotweezers for Interrogating Biological Processes in Space and Time. *Acc. Chem. Res.* **2018**, *51*, 839–849.
- (22) Rivera-Rodriguez, A.; Hoang-Minh, L. B.; Chiu-Lam, A.; Sarna, N.; Marrero-Morales, L.; Mitchell, D. A.; Rinaldi-Ramos, C. M. Tracking Adoptive T Cell Immunotherapy Using Magnetic Particle Imaging. *Nanotheranostics* **2021**, *5*, 431–444.
- (23) Felfoul, O.; Mohammadi, M.; Taherkhani, S.; de Lanauze, D.; Zhong Xu, Y.; Loghin, D.; Essa, S.; Jancik, S.; Houle, D.; Lafleur, M.; Gaboury, L.; Tabrizian, M.; Kaou, N.; Atkin, M.; Vuong, T.; Batist, G.; Beauchemin, N.; Radzioch, D.; Martel, S. Magneto-Aerotactic Bacteria Deliver Drug-Containing Nanoliposomes to Tumour Hypoxic Regions. *Nat. Nanotechnol.* **2016**, *11*, 941–947.
- (24) Schuerle, S.; Soleimany, A. P.; Yeh, T.; Anand, G. M.; Häberli, M.; Fleming, H. E.; Mirkhani, N.; Qiu, F.; Hauert, S.; Wang, X.; Nelson, B. J.; Bhatia, S. N. Synthetic and Living Micropropellers for Convection-Enhanced Nanoparticle Transport. *Sci. Adv.* **2019**, *5*, No. eaav4803.
- (25) Yang, L.; Yu, J.; Zhang, L. Statistics-Based Automated Control for a Swarm of Paramagnetic Nanoparticles in 2-D Space. *IEEE Trans. Robot.* **2020**, *36*, 254–270.
- (26) Wang, X.; Ho, C.; Tsatskis, Y.; Law, J.; Zhang, Z.; Zhu, M.; Dai, C.; Wang, F.; Tan, M.; Hopyan, S.; McNeill, H.; Sun, Y. Intracellular Manipulation and Measurement with Multipole Magnetic Tweezers. *Sci. Robot.* **2019**, *4*, No. eaav6180.
- (27) Schuerle, S.; Vizcarra, I. A.; Moeller, J.; Sakar, M. S.; Özkale, B.; Lindo, A. M. H.; Mushtaq, F.; Schoen, I.; Pané, S.; Vogel, V.; Nelson, B. J. Robotically Controlled Micropropy to Resolve Initial Attack Modes Preceding Phagocytosis. *Sci. Robot.* **2017**, *2*, No. eaah6094.
- (28) de Vries, A. H. B.; Krenn, B. E.; van Driel, R.; Subramaniam, V.; Kanger, J. S. Direct Observation of Nanomechanical Properties of Chromatin in Living Cells. *Nano Lett.* **2007**, *7*, 1424–1427.
- (29) Ahmed, D.; Baasch, T.; Blondel, N.; Läubli, N.; Dual, J.; Nelson, B. J. Neutrophil-Inspired Propulsion in a Combined Acoustic and Magnetic Field. *Nat. Commun.* **2017**, *8*, 770.
- (30) Servant, A.; Qiu, F.; Mazza, M.; Kostarelos, K.; Nelson, B. J. Controlled in Vivo Swimming of a Swarm of Bacteria-like Microbotic Flagella. *Adv. Mater.* **2015**, *27*, 2981–2988.
- (31) Xie, H.; Sun, M.; Fan, X.; Lin, Z.; Chen, W.; Wang, L.; Dong, L.; He, Q. Reconfigurable Magnetic Microrobot Swarm: Multimode Transformation, Locomotion, and Manipulation. *Sci. Robot.* **2019**, *4*, No. eaav8006.
- (32) Yu, J.; Yang, L.; Zhang, L. Pattern Generation and Motion Control of a Vortex-like Paramagnetic Nanoparticle Swarm. *Int. J. Rob. Res.* **2018**, *37*, 912–930.
- (33) Wang, Q.; Yang, L.; Yu, J.; Vong, C. I.; Yan Chiu, P. W.; Zhang, L. Magnetic Navigation of a Rotating Colloidal Swarm Using Ultrasound Images. *2018 IEEE/RSJ. International Conference on Intelligent Robots and Systems (IROS)* **2018**, 5380–5385.
- (34) Wang, X.; Luo, M.; Wu, H.; Zhang, Z.; Liu, J.; Xu, Z.; Johnson, W.; Sun, Y. A Three-Dimensional Magnetic Tweezer System for Intraembryonic Navigation and Measurement. *IEEE Trans. Robot.* **2018**, *34*, 240–247.

- (35) Zhang, Z.; Wang, X.; Liu, J.; Dai, C.; Sun, Y. Robotic Micromanipulation: Fundamentals and Applications. *Annu. Rev. Control Robot. Auton. Syst.* **2019**, *2*, 181–203.
- (36) Singh, A. V.; Laux, P.; Luch, A.; Sudrik, C.; Wiehr, S.; Wild, A. M.; Santomauro, G.; Bill, J.; Sitti, M. Review of Emerging Concepts in Nanotoxicology: Opportunities and Challenges for Safer Nanomaterial Design. *Toxicol. Mech. Methods* **2019**, *29*, 378–387.
- (37) Kroll, A.; Pillukat, M. H.; Hahn, D.; Schnekenburger, J. Interference of Engineered Nanoparticles with in Vitro Toxicity Assays. *Arch. Toxicol.* **2012**, *86*, 1123–1136.
- (38) Landsiedel, R.; Ma-Hock, L.; Kroll, A.; Hahn, D.; Schnekenburger, J.; Wiench, K.; Wohlleben, W. Testing Metal-Oxide Nanomaterials for Human Safety. *Adv. Mater.* **2010**, *22*, 2601–2627.
- (39) Behzadi, S.; Serpooshan, V.; Tao, W.; Hamaly, M. A.; Alkawareek, M. Y.; Dreaden, E. C.; Brown, D.; Alkilany, A. M.; Farokhzad, O. C.; Mahmoudi, M. Cellular Uptake of Nanoparticles: Journey inside the Cell. *Chem. Soc. Rev.* **2017**, *46*, 4218–4244.
- (40) Kettler, K.; Veltman, K.; van de Meent, D.; van Wezel, A.; Hendriks, A. J. Cellular Uptake of Nanoparticles as Determined by Particle Properties, Experimental Conditions, and Cell Type. *Environ. Toxicol. Chem.* **2014**, *33*, 481–492.
- (41) Duan, X.; Li, Y. Physicochemical Characteristics of Nanoparticles Affect Circulation, Biodistribution, Cellular Internalization, and Trafficking. *Small* **2013**, *9*, 1521–1532.
- (42) Venugopalan, P. L.; Esteban-Fernández De Ávila, B.; Pal, M.; Ghosh, A.; Wang, J. Fantastic Voyage of Nanomotors into the Cell. *ACS Nano* **2020**, *14*, 9423–9439.
- (43) Zhang, Z.; Huang, K.; Menq, C. H. Design, Implementation, and Force Modeling of Quadrupole Magnetic Tweezers. *IEEE/ASME Trans. Mechatronics* **2010**, *15*, 704–713.
- (44) de Vries, A. H. B.; Krenn, B. E.; van Driel, R.; Kanger, J. S. Micro Magnetic Tweezers for Nanomanipulation inside Live Cells. *Biophys. J.* **2005**, *88*, 2137–2144.
- (45) Zhang, Z.; Huang, Y.; Menq, C. H. Actively Controlled Manipulation of a Magnetic Microbead Using Quadrupole Magnetic Tweezers. *IEEE Trans. Robot.* **2010**, *26*, 531–541.
- (46) Zarrouk, A.; Belharet, K.; Tahri, O.; Ferreira, A. A Four-Magnet System for 2D Wireless Open-Loop Control of Microrobots. *2019 IEEE International Conference on Robotics and Automation (ICRA)* **2019**, 883–888.
- (47) Yigit, B.; Alapan, Y.; Sitti, M. Cohesive Self-Organization of Mobile Microrobotic Swarms. *Soft Matter* **2020**, *16*, 1996–2004.
- (48) Petrie, R. J.; Yamada, K. M. At the Leading Edge of Three-Dimensional Cell Migration. *J. Cell Sci.* **2012**, *125*, S917–S926.
- (49) Lauffenburger, D. A.; Horvitz, A. F. Cell Migration: A Physically Integrated Molecular Process. *Cell* **1996**, *84*, 359–369.
- (50) Martin, C.; Pedersen, S. F.; Schwab, A.; Stock, C. Intracellular PH Gradients in Migrating Cells. *Am. J. Physiol., Cell Physiol.* **2011**, *300*, C490–C495.
- (51) Stüwe, L.; Müller, M.; Fabian, A.; Waning, J.; Mally, S.; Noël, J.; Schwab, A.; Stock, C. PH Dependence of Melanoma Cell Migration: Protons Extruded by NHE1 Dominate Protons of the Bulk Solution. *J. Physiol.* **2007**, *585*, 351–360.
- (52) Tarbashevich, K.; Reichman-Fried, M.; Grimaldi, C.; Raz, E. Chemokine-Dependent PH Elevation at the Cell Front Sustains Polarity in Directionally Migrating Zebrafish Germ Cells. *Curr. Biol.* **2015**, *25*, 1096–1103.
- (53) Stüwe, L.; Müller, M.; Fabian, A.; Waning, J.; Mally, S.; Noël, J.; Schwab, A.; Stock, C. PH Dependence of Melanoma Cell Migration: Protons Extruded by NHE1 Dominate Protons of the Bulk Solution. *J. Physiol.* **2007**, *585*, 351–360.
- (54) Hall, R. A.; Vullo, D.; Innocenti, A.; Scozzafava, A.; Supuran, C. T.; Klappa, P.; Mühlischlegel, F. A. External PH Influences the Transcriptional Profile of the Carbonic Anhydrase, CAH-4b in *Caenorhabditis Elegans*. *Mol. Biochem. Parasitol.* **2008**, *161*, 140–149.
- (55) van Voorhies, W. A.; Fuchs, J.; Thomas, S. The Longevity of *Caenorhabditis Elegans* in Soil. *Biol. Lett.* **2005**, *1*, 247–249.
- (56) Rieckher, M.; Tavernarakis, N. Generation of *Caenorhabditis Elegans* Transgenic Animals by DNA Microinjection. *Bio-Protoc.* **2017**, *7*, 2565.
- (57) Surana, S.; Bhat, J. M.; Koushika, S. P.; Krishnan, Y. An Autonomous DNA Nanomachine Maps Spatiotemporal PH Changes in a Multicellular Living Organism. *Nat. Commun.* **2011**, *2*, 340.
- (58) Garzon-Coral, C.; Fantana, H. A.; Howard, J. A Force-Generating Machinery Maintains the Spindle at the Cell Center during Mitosis. *Science* **2016**, *352*, 1124–1127.
- (59) Grant, J.; Matthewman, C.; Bianchi, L. A Novel Mechanism of PH Buffering in *c. Elegans* Glia: Bicarbonate Transport via the Voltage-Gated ClC Cl Channel CLH-1. *J. Neurosci.* **2015**, *35*, 16377–16397.
- (60) Cong, Y.; Yang, H.; Zhang, P.; Xie, Y.; Cao, X.; Zhang, L. Transcriptome Analysis of the Nematode *Caenorhabditis Elegans* in Acidic Stress Environments. *Front. Physiol.* **2020**, *11*, 1107.
- (61) Munaron, L.; Antoniotti, S.; Lovisolo, D. Intracellular Calcium Signals and Control of Cell Proliferation: How Many Mechanisms? *J. Cell. Mol. Med.* **2004**, *8*, 161–168.
- (62) Rodrigues, M. A.; Gomes, D. A.; Leite, M. F.; Grant, W.; Zhang, L.; Lam, W.; Cheng, Y. C.; Bennett, A. M.; Nathanson, M. H. Nucleoplasmic Calcium Is Required for Cell Proliferation. *J. Biol. Chem.* **2007**, *282*, 17061–17068.
- (63) Pinto, M. C. X.; Kihara, A. H.; Goulart, V. A. M.; Tonelli, F. M. P.; Gomes, K. N.; Ulrich, H.; Resende, R. R. Calcium Signaling and Cell Proliferation. *Cell. Signalling* **2015**, *27*, 2139–2149.
- (64) Resende, R. R.; Andrade, L. M.; Oliveira, A. G.; Guimarães, E. S.; Guatimosim, S.; Leite, M. F. Nucleoplasmic Calcium Signaling and Cell Proliferation: Calcium Signaling in the Nucleus. *Cell Commun. Signaling* **2013**, *11*, 14.
- (65) Berridge, M. J. Calcium Signalling and Cell Proliferation. *BioEssays* **1995**, *17*, 491–500.
- (66) MartíRuiz, M. C.; Hubbard, K. E.; Gardner, M. J.; Jung, H. J.; Aubry, S.; Hotta, C. T.; Mohd-Noh, N. I.; Robertson, F. C.; Hearn, T. J.; Tsai, Y. C.; Dodd, A. N.; Hannah, M.; Carré, I. A.; Davies, J. M.; Braam, J.; Webb, A. A. R. Circadian Oscillations of Cytosolic Free Calcium Regulate the Arabidopsis Circadian Clock. *Nat. Plants* **2018**, *4*, 690–698.
- (67) Galon, Y.; Finkler, A.; Fromm, H. Calcium-Regulated Transcription in Plants. *Mol. Plant* **2010**, *3*, 653–669.
- (68) Wiegert, J. S.; Bading, H. Activity-Dependent Calcium Signaling and ERK-MAP Kinases in Neurons: A Link to Structural Plasticity of the Nucleus and Gene Transcription Regulation. *Cell Calcium* **2011**, *49*, 296–305.
- (69) Reddy, A. S. N.; Ali, G. S.; Celesnik, H.; Day, I. S. Coping with Stresses: Roles of Calcium- and Calcium/Calmodulin-Regulated Gene Expression. *Plant Cell* **2011**, *23*, 2010–2032.
- (70) Machaca, K. Ca<sup>2+</sup> Signaling, Genes and the Cell Cycle. *Cell Calcium* **2011**, *49*, 323–330.
- (71) Nomura, M.; Ueno, A.; Saga, K.; Fukuzawa, M.; Kaneda, Y. Accumulation of Cytosolic Calcium Induces Necroptotic Cell Death in Human Neuroblastoma. *Cancer Res.* **2014**, *74*, 1056–1066.
- (72) Orrenius, S.; Gogvadze, V.; Zhivotovsky, B. Calcium and Mitochondria in the Regulation of Cell Death. *Biochem. Biophys. Res. Commun.* **2015**, *460*, 72–81.
- (73) Zhivotovsky, B.; Orrenius, S. Calcium and Cell Death Mechanisms: A Perspective from the Cell Death Community. *Cell Calcium* **2011**, *50*, 211–221.
- (74) de Felice, D.; Alaimo, A. Mechanosensitive Piezo Channels in Cancer: Focus on Altered Calcium Signaling in Cancer Cells and in Tumor Progression. *Cancers* **2020**, *12* (7), 1780.
- (75) Chen, X.; Wanggou, S.; Bodalia, A.; Zhu, M.; Dong, W.; Fan, J. J.; Yin, W. C.; Min, H. K.; Hu, M.; Draghici, D.; Dou, W.; Li, F.; Coutinho, F. J.; Whetstone, H.; Kushida, M. M.; Dirks, P. B.; Song, Y.; Hui, C. chung; Sun, Y.; Wang, L. Y.; Li, X.; Huang, X. A Feedforward Mechanism Mediated by Mechanosensitive Ion Channel PIEZO1 and Tissue Mechanics Promotes Glioma Aggression. *Neuron* **2018**, *100* (4), 799–815.

(76) Ljubojevic, S.; Radulovic, S.; Leitinger, G.; Sedej, S.; Sacherer, M.; Holzer, M.; Winkler, C.; Pritz, E.; Mittler, T.; Schmidt, A.; Sereinigg, M.; Wakula, P.; Zissimopoulos, S.; Bisping, E.; Post, H.; Marsche, G.; Bossuyt, J.; Bers, D. M.; Kockskämper, J.; Pieske, B. Early Remodeling of Perinuclear Ca<sup>2+</sup> Stores and Nucleoplasmic Ca<sup>2+</sup> Signaling during the Development of Hypertrophy and Heart Failure. *Circulation* **2014**, *130*, 244–255.

(77) Ferrier, J.; Yu, H. Nuclear versus Perinuclear and Cytoplasmic Calcium in Osteoclasts. *Cell Calcium* **1996**, *20*, 381–388.

(78) Shimojima, M.; Yuasa, S.; Motoda, C.; Yozu, G.; Nagai, T.; Ito, S.; Lachmann, M.; Kashimura, S.; Takei, M.; Kusumoto, D.; Kunitomi, A.; Hayashiji, N.; Seki, T.; Tohyama, S.; Hashimoto, H.; Kodaira, M.; Egashira, T.; Hayashi, K.; Nakanishi, C.; Sakata, K.; Yamagishi, M.; Fukuda, K. Emerin Plays a Crucial Role in Nuclear Invagination and in the Nuclear Calcium Transient. *Sci. Rep.* **2017**, *7*, 44312.

(79) Allbritton, N. L.; Oancea, E.; Kuhn, M. A.; Meyer, T. Source of Nuclear Calcium Signals. *Proc. Natl. Acad. Sci. U. S. A.* **1994**, *91*, 12458–12462.

(80) Momin, A.; Bahrapour, S.; Min, H. K.; Chen, X.; Wang, X.; Sun, Y.; Huang, X. Channeling Force in the Brain: Mechanosensitive Ion Channels Choreograph Mechanics and Malignancies. *Trends Pharmacol. Sci.* **2021**, *42*, 367–384.

(81) Ibarra, C.; Vicencio, J. M.; Estrada, M.; Lin, Y.; Rocco, P.; Rebellato, P.; Munoz, J. P.; Garcia-Prieto, J.; Quest, A. F. G.; Chiong, M.; Davidson, S. M.; Bulatovic, I.; Grinnemo, K. H.; Larsson, O.; Szabadkai, G.; Uhlén, P.; Jaimovich, E.; Lavandero, S. Local Control of Nuclear Calcium Signaling in Cardiac Myocytes by Perinuclear Microdomains of Sarcolemmal Insulin-like Growth Factor 1 Receptors. *Circ. Res.* **2013**, *112*, 236–245.

(82) Bagur, R.; Hajnóczky, G. Intracellular Ca<sup>2+</sup> Sensing: Its Role in Calcium Homeostasis and Signaling. *Mol. Cell* **2017**, *66*, 780–788.

(83) Kim, T. J.; Joo, C.; Seong, J.; Vafabakhsh, R.; Botvinick, E. L.; Berns, M. W.; Palmer, A. E.; Wang, N.; Ha, T.; Jakobsson, E.; Sun, J.; Wang, Y. Distinct Mechanisms Regulating Mechanical Force-Induced Ca<sup>2+</sup> Signals at the Plasma Membrane and the ER in Human MSCs. *Elife* **2015**, *4*, e04876.

(84) Santana, D.; Malik, A. B.; Mehta, D.; Komarova, Y. A. Role of Piezo1 in CAMP-Dependent Calcium Release From ER Stores in Endothelial Cells. *FASEB J.* **2019**, *33*, 809.

(85) Nair, A.; Chauhan, P.; Saha, B.; Kubatzky, K. F. Conceptual Evolution of Cell Signaling. *Int. J. Mol. Sci.* **2019**, *20*, 3292.

(86) Maharramov, A. M.; Mahmudov, K. T.; Kopylovich, M. N.; Pombeiro, A. J. L. *Non-Covalent Interactions in the Synthesis and Design of New Compounds*; John Wiley & Sons, Inc.: Hoboken, NJ, 2016.

(87) Pan, J.; Liu, N.; Shu, L.; Sun, H. Application of Avidin-Biotin Technology to Improve Cell Adhesion on Nanofibrous Matrices. *J. Nanobiotechnol.* **2015**, *13*, 37.

(88) Peerzade, S. A. M. A.; Makarova, N.; Sokolov, I. Ultrabright Fluorescent Silica Nanoparticles for Dual Ph and Temperature Measurements. *Nanomaterials* **2021**, *11*, 1524.

(89) Rappel, W. J.; Edelstein-Keshet, L. Mechanisms of Cell Polarization. *Curr. Opin. Syst. Biol.* **2017**, *3*, 43–53.

(90) Lee, R. M.; Stuelten, C. H.; Parent, C. A.; Losert, W. Collective Cell Migration over Long Time Scales Reveals Distinct Phenotypes. *Convergent Sci. Phys. Oncol.* **2016**, *2*, 025001.

(91) Pollard, S. M.; Yoshikawa, K.; Clarke, I. D.; Danovi, D.; Stricker, S.; Russell, R.; Bayani, J.; Head, R.; Lee, M.; Bernstein, M.; Squire, J. A.; Smith, A.; Dirks, P. Glioma Stem Cell Lines Expanded in Adherent Culture Have Tumor-Specific Phenotypes and Are Suitable for Chemical and Genetic Screens. *Cell Stem Cell* **2009**, *4*, 568–580.

(92) Liu, J.; Siragam, V.; Gong, Z.; Chen, J.; Fridman, M. D.; Leung, C.; Lu, Z.; Ru, C.; Xie, S.; Luo, J.; Hamilton, R. M.; Sun, Y. Robotic Adherent Cell Injection for Characterizing Cell-Cell Communication. *IEEE Trans. Biomed. Eng.* **2015**, *62*, 119–125.

(93) Merrill, R. A.; Flippo, K. H.; Strack, S. Measuring mitochondrial shape with ImageJ. In *Techniques to Investigate Mitochondrial Function in Neurons*; Strack, S., Usachev, Y. M., Eds.; Humana Press: New York, 2017; pp 31–48.

## Recommended by ACS

### A pH-Reversible Fluorescent Probe for in Situ Imaging of Extracellular Vesicles and Their Secretion from Living Cells

Hanzhuang Liu, Chung Hang Jonathan Choi, *et al.*

NOVEMBER 01, 2021  
NANO LETTERS

READ 

### A Class of Biocompatible Dye-Protein Complex Optical Nanoprobes

Xindong Wang, Guanying Chen, *et al.*

DECEMBER 23, 2021  
ACS NANO

READ 

### Dynamic Heterochromatin States in Anisotropic Nuclei of Cells on Aligned Nanofibers

Wenjie Liu, Joseph Irudayaraj, *et al.*

JULY 08, 2022  
ACS NANO

READ 

### Oxygen Quenching-Resistant Nanoaggregates with Aggregation-Induced Delayed Fluorescence for Time-Resolved Mapping of Intracellular Microviscosity

Fengyan Song, Ben Zhong Tang, *et al.*

MARCH 23, 2022  
ACS NANO

READ 

Get More Suggestions >